Supporting Information

Supersensitive Detection of Anions in Pure Organic and Aqueous Media by Amino Acids Conjugated Ellman's Reagent

Sameer Dhawan,[a] Harsha Devnani,[a] Jisha Babu,[a] Hanuman Singh,[a] M. Ali Haider,[b] Tuhin S. Khan,[c] Pravin P. Ingole*[a] and V. Haridas*[a]*

[a]Department of Chemistry, Indian Institute of Technology Delhi, New Delhi-110016, India.

[b]Renewable Energy and Chemicals Laboratory, Department of Chemical Engineering, Indian Institute of Technology Delhi, New Delhi-110016, India.

[c]Light Stock Processing Division, CSIR-Indian Institute of Petroleum, Dehradun, 248005, India.

∗ Corresponding authors:

E-mail: haridasv@chemistry.iitd.ac.in
Tel.: +91-11-2659 1380

E-mail: ppingole@chemistry.iitd.ac.in
Tel.: +91-11-2659 7538

E-mail: tuhins.khan@iip.res.in
Tel.: +91-13-5252 5915

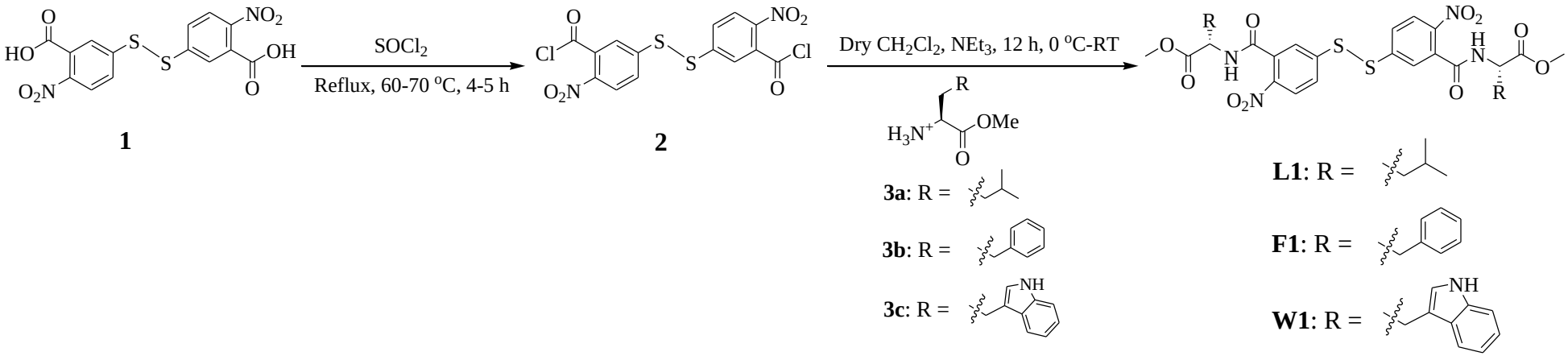

Scheme S1: Synthesis of Ellman's reagent-cored hosts **L1**, **F1** and **W1**.

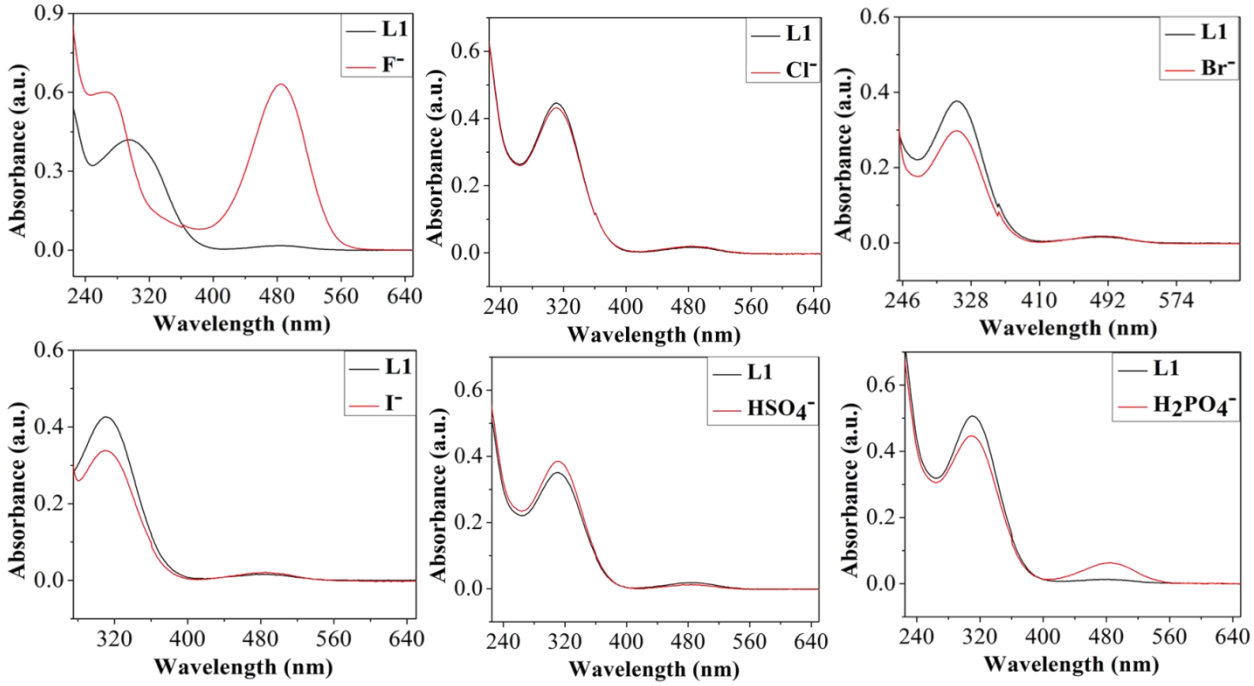

Figure S1: An initial screening of anion binding potential of **L1** upon addition of 50 equiv. of various anions.

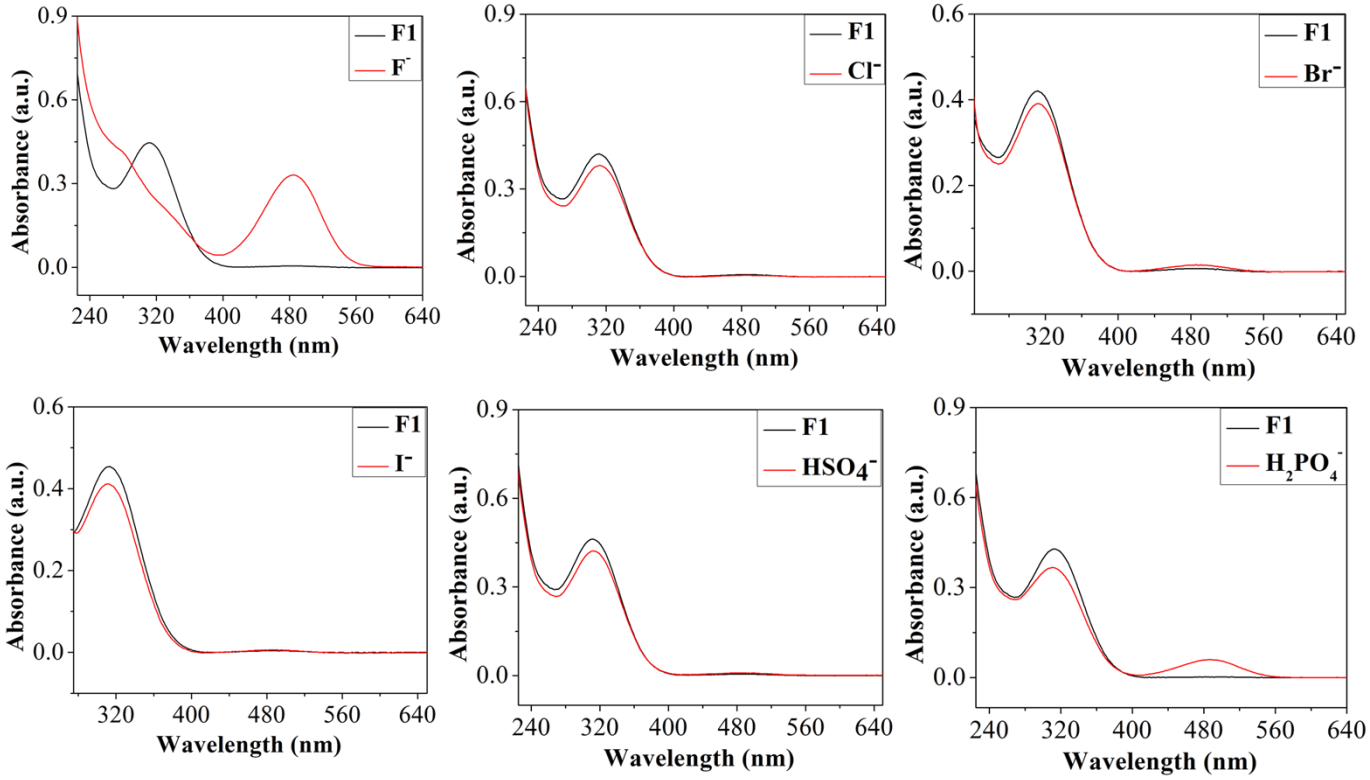

Figure S2: An initial screening of anion binding potential of **F1** upon addition of 50 equiv. of various anions.

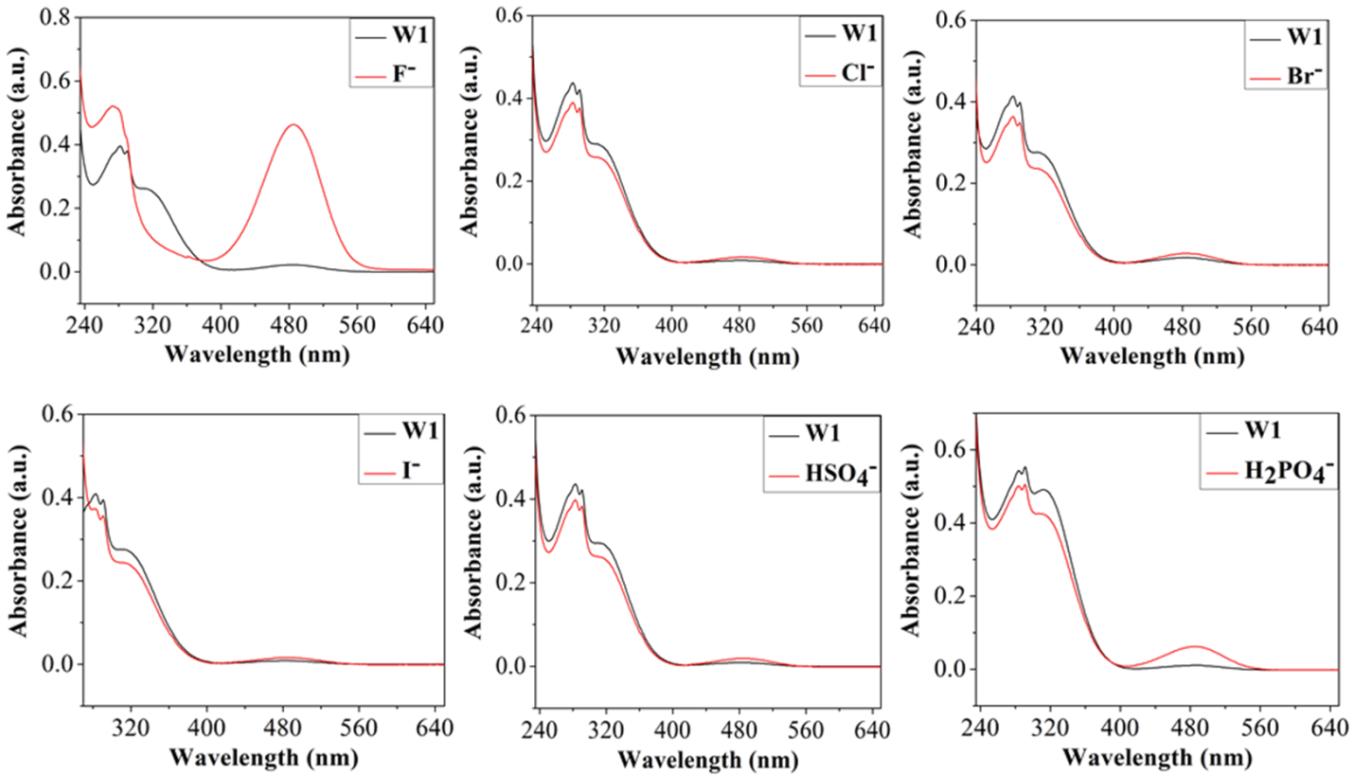

Figure S3: An initial screening of anion binding potential of **W1** upon addition of 50 equiv. of various anions.

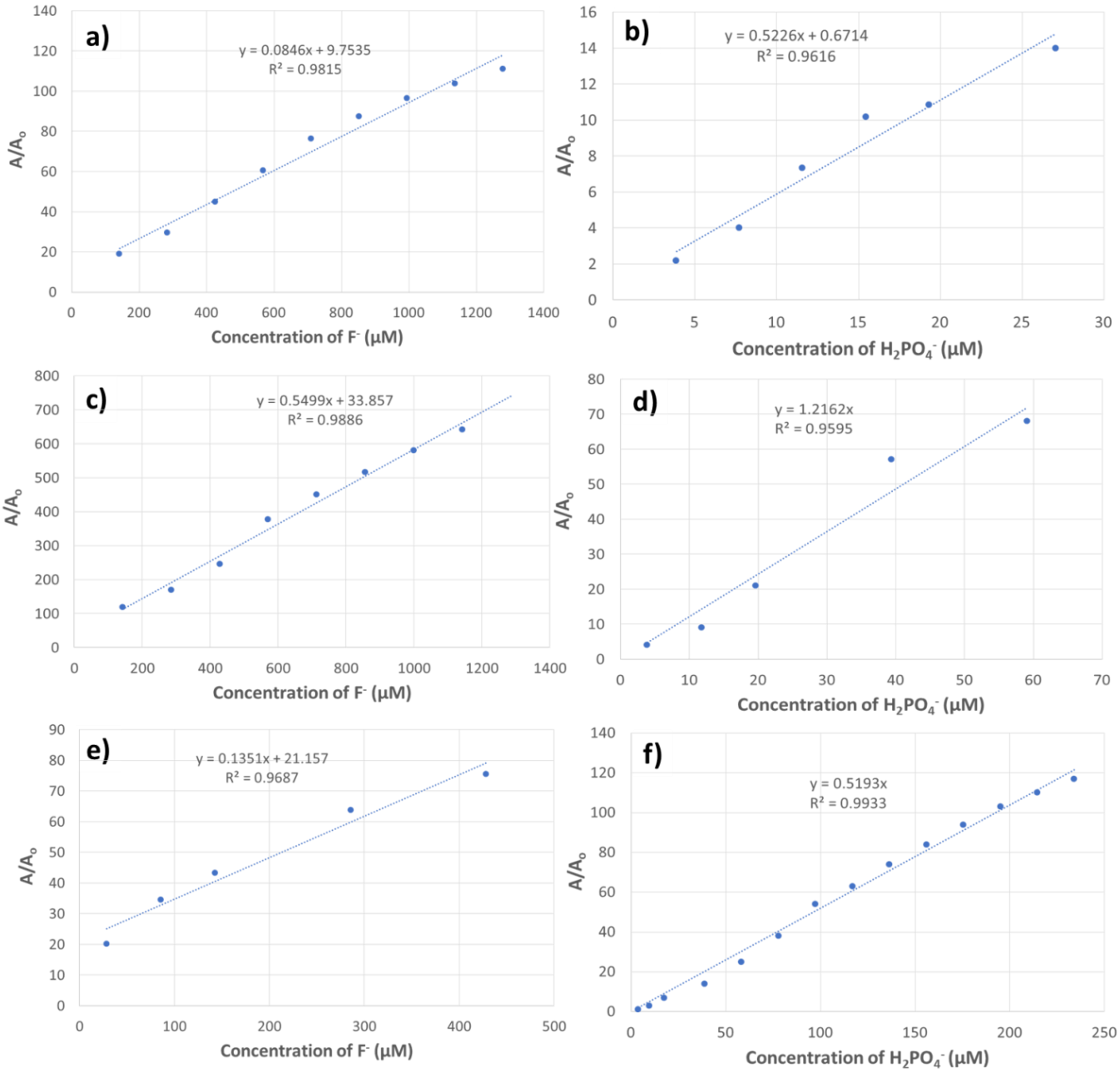

Figure S4: Determination of LOD of chemosensors with anions. a) **L1** with F^-, b) **L1** with $H_2PO_4^-$, c) **F1** with F^-, d) **F1** with $H_2PO_4^-$, e) **W1** with F^-, f) **W1** with $H_2PO_4^-$.

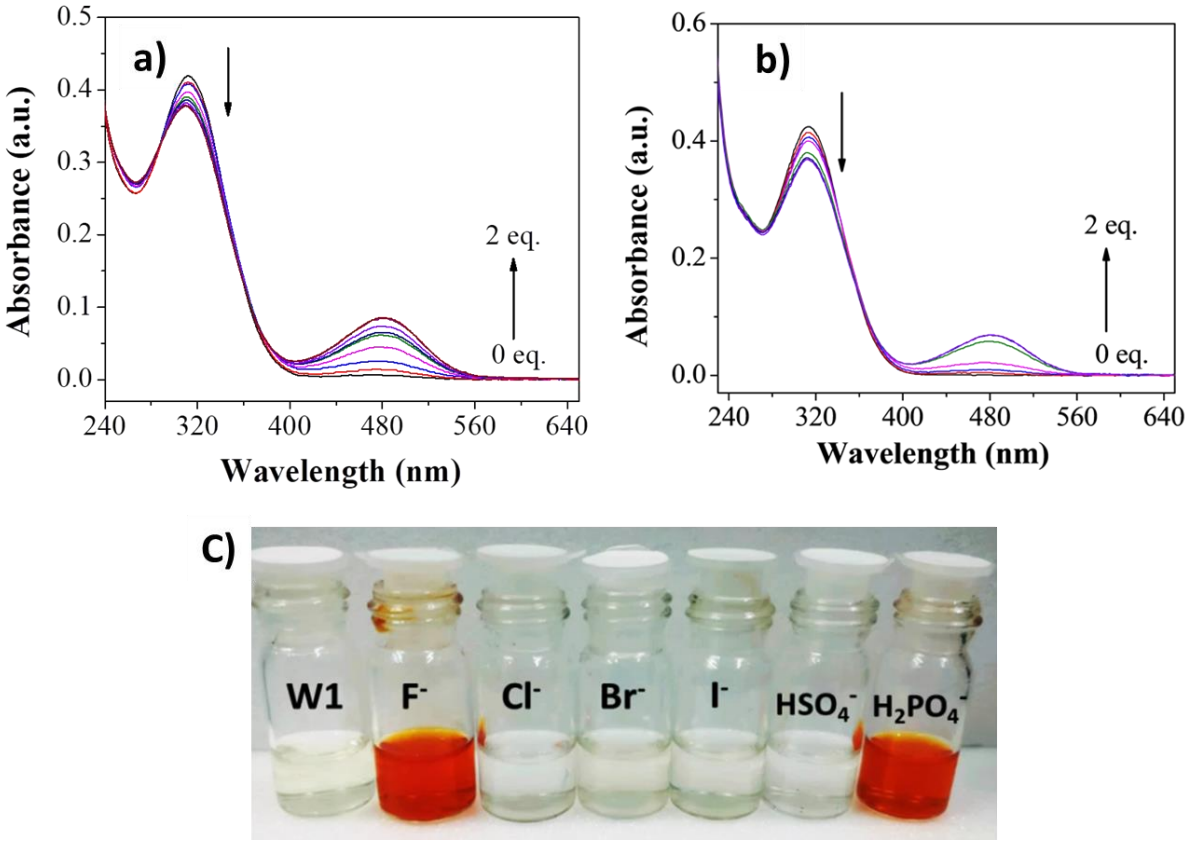

Figure S5: UV-vis titration profile of a) **L1** against $H_2PO_4^-$, b) **F1** against $H_2PO_4^-$; c) colorimetric response of **W1** upon addition of different anions.

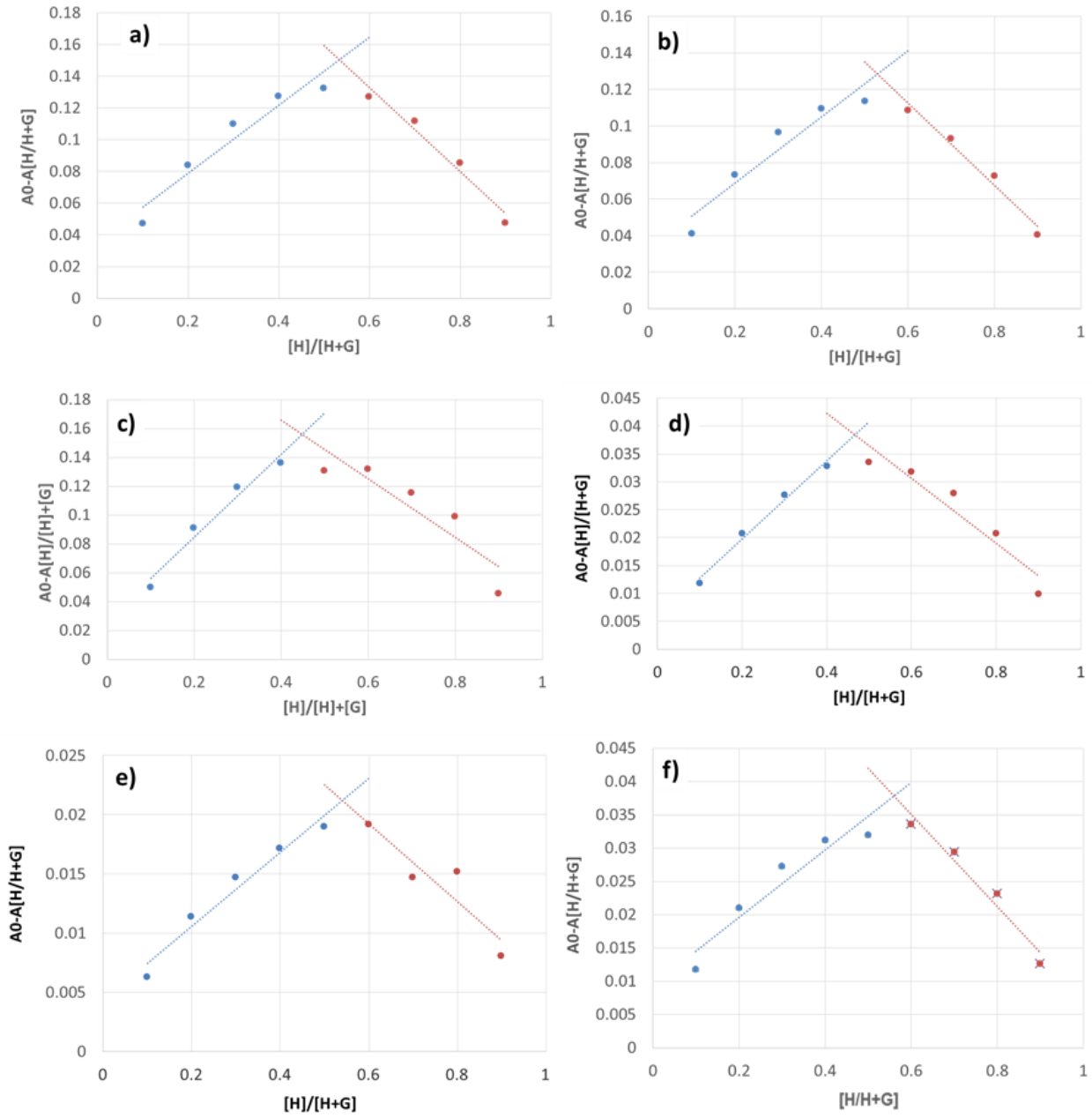

Figure S6: Job plots of host with anions a) **L1** with F^-, b) **F1** with F^-, c) **W1** with F^-, d) **L1** with $H_2PO_4^-$, e) **F1** with $H_2PO_4^-$, f) **W1** with $H_2PO_4^-$.

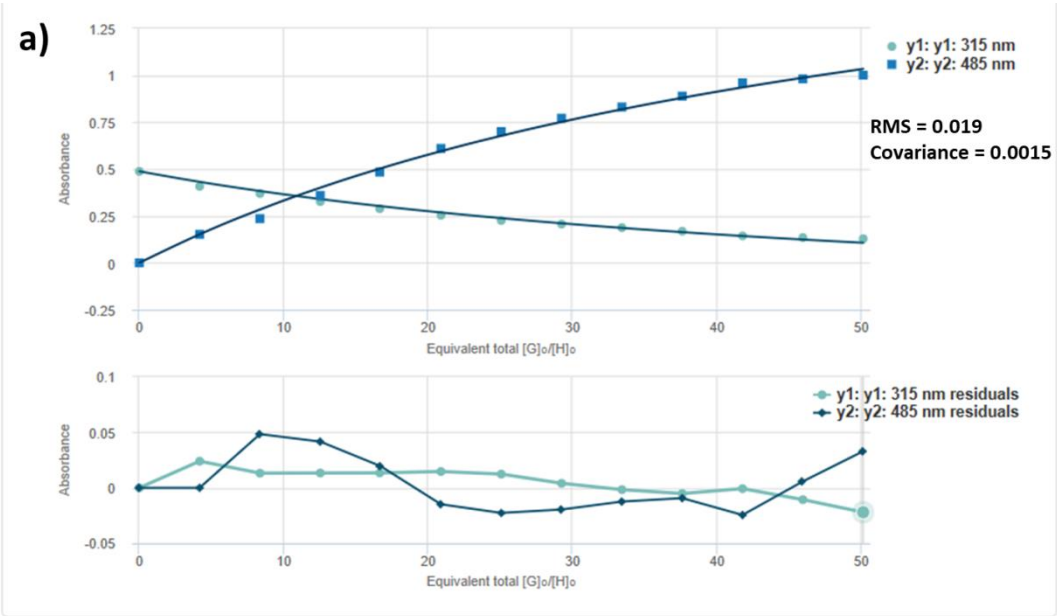

http://app.supramolecular.org/bindfit/view/73644b71-a124-45cf-ba54-1dd963748299

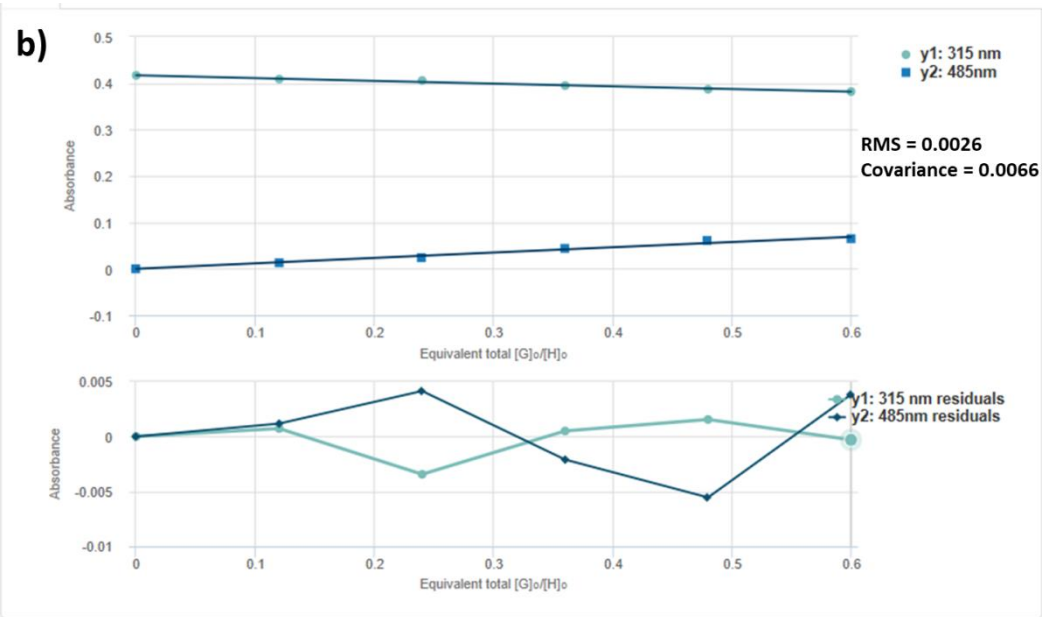

http://app.supramolecular.org/bindfit/view/e77832b0-6922-460f-b31b-bd5b6cc939e1

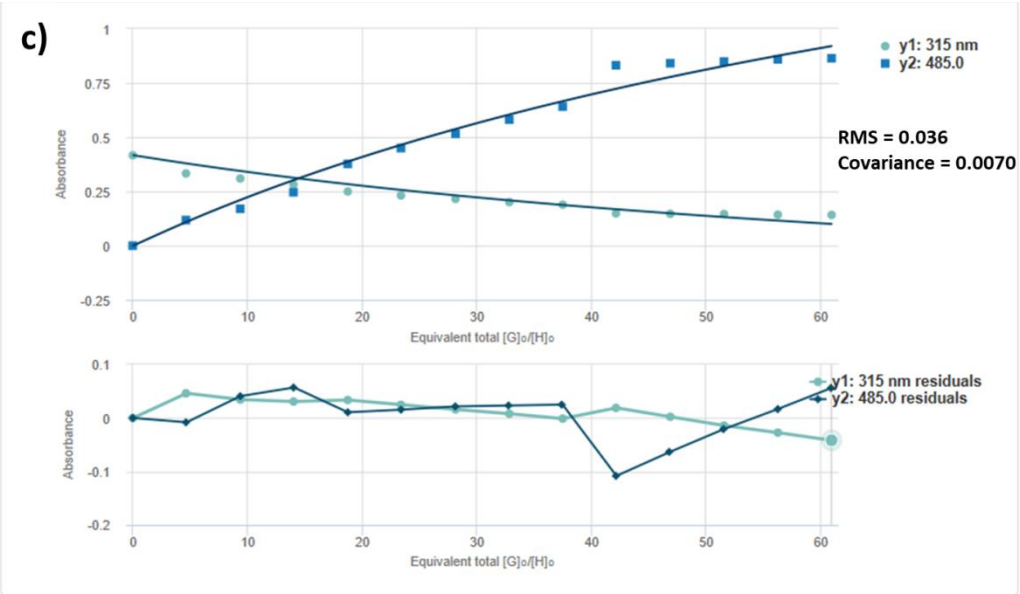

http://app.supramolecular.org/bindfit/view/219338d4-4f4d-4aa7-8e4e-c096950c1981

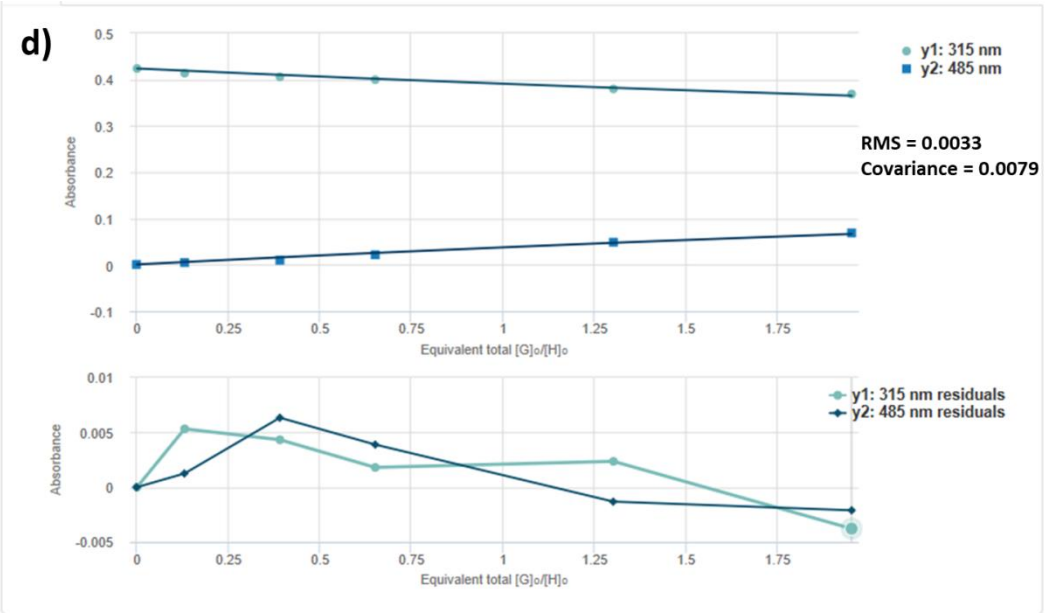

http://app.supramolecular.org/bindfit/view/bede5de5-4d69-4e94-8739-6615ffc1ad43

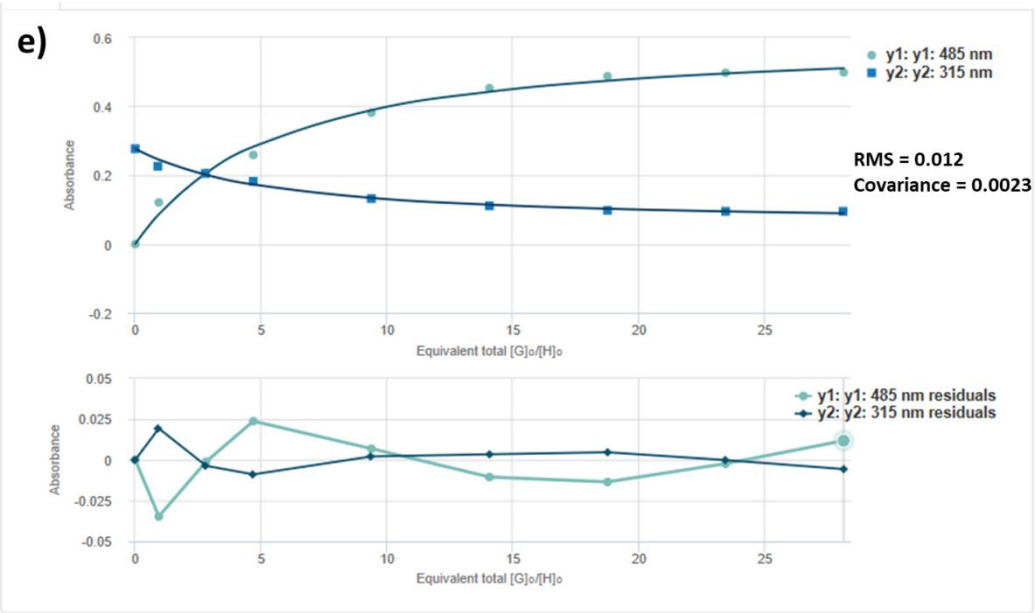

http://app.supramolecular.org/bindfit/view/80868222-fafa-4856-856f-d67753286211

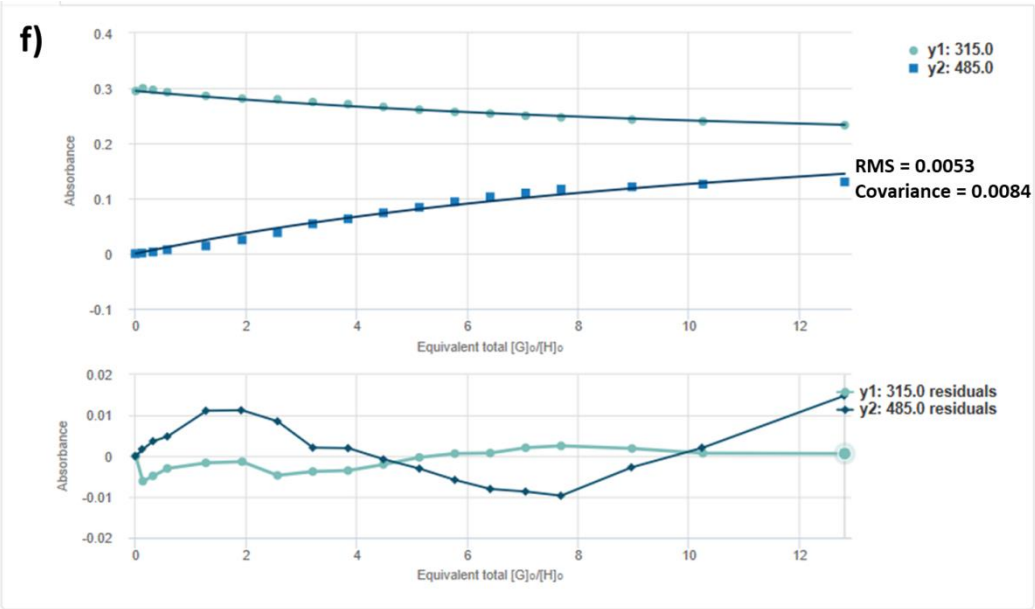

http://app.supramolecular.org/bindfit/view/f99903be-2415-403a-8f0f-d72ba62a245a

Figure S7: Fitting and residual plots for UV-vis titrations as obtained from BindFit a) **L1** with F^-, b) **L1** with $H_2PO_4^-$, c) **F1** with F^-, d) **F1** with $H_2PO_4^-$ e) **W1** with F^-, f) **W1** with $H_2PO_4^-$. BindFit URLs are given corresponding to each titration.

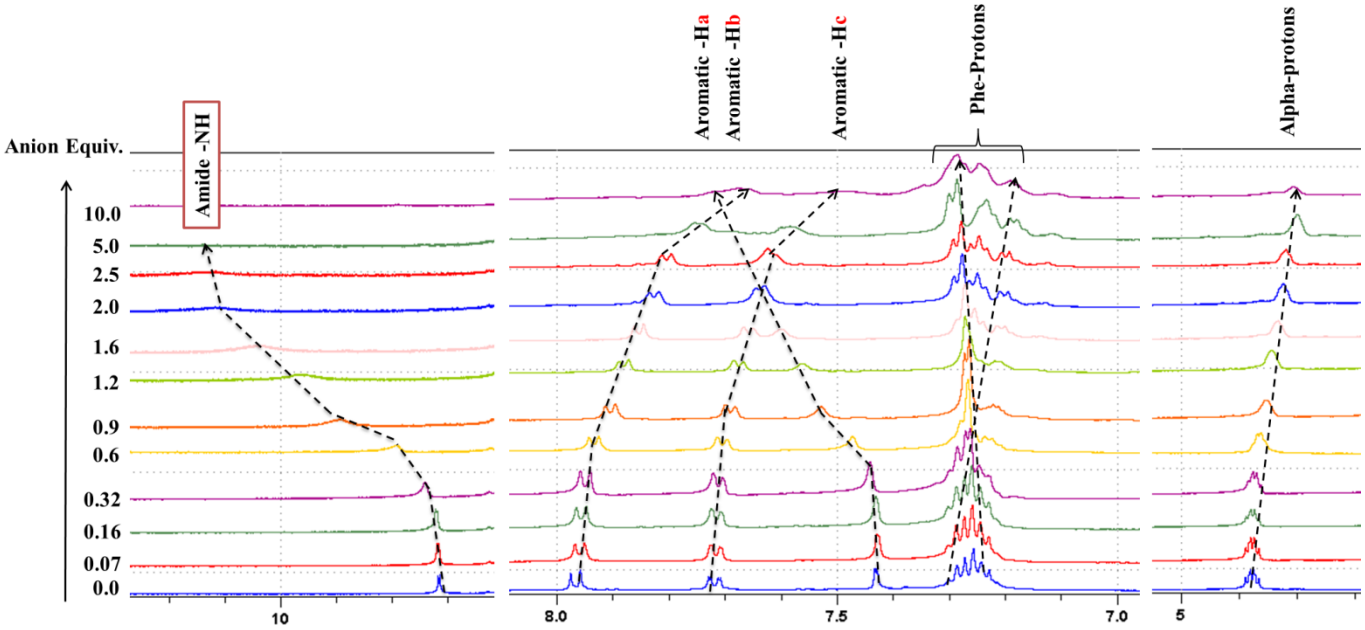

Figure S8: Stack plots of ^{1}H NMR spectra (500 MHz, CD_3CN:DMSO-d_6 9:1) of **F1** with increasing amount of TBAF. The region of protons involved in the binding is shown.

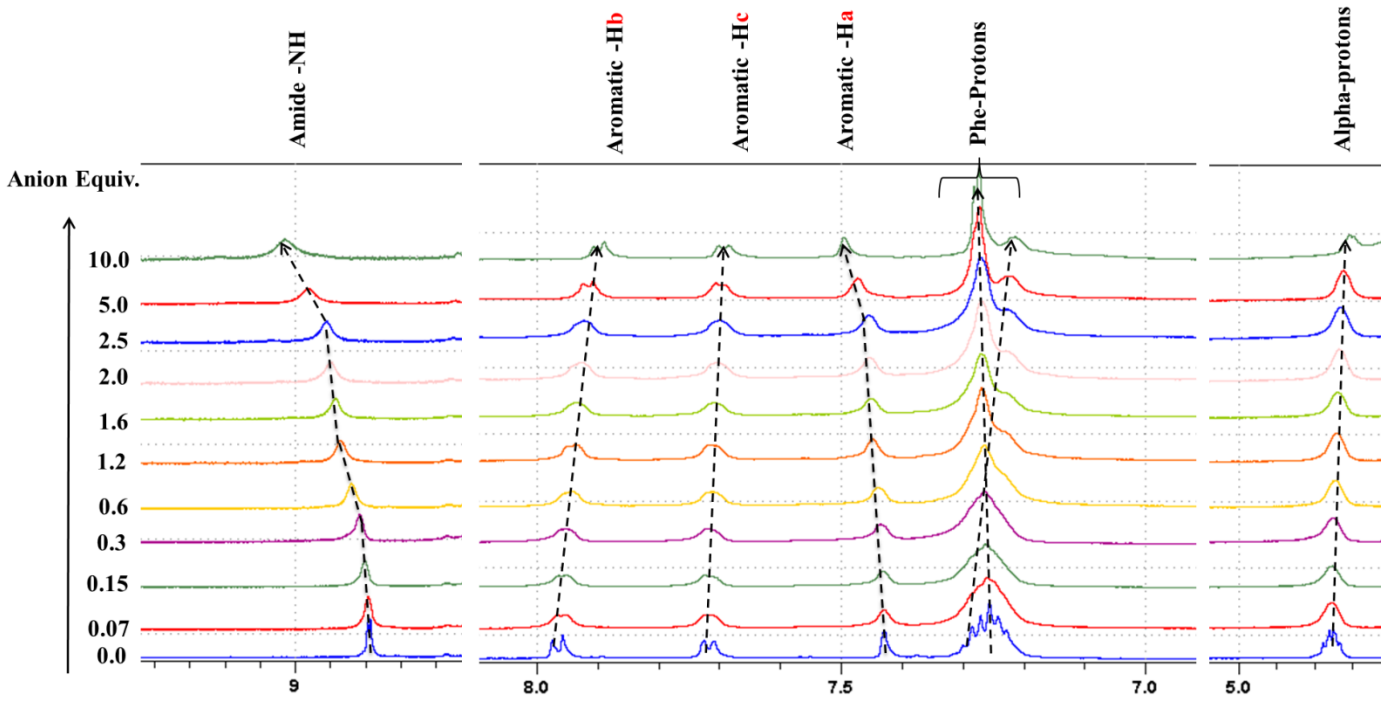

Figure S9: Stack plots of ^{1}H NMR spectra (500 MHz, CD_3CN:DMSO-d_6 9:1) of **F1** with increasing amount of $TBAH_2PO_4$. The region of protons involved in the binding is shown.

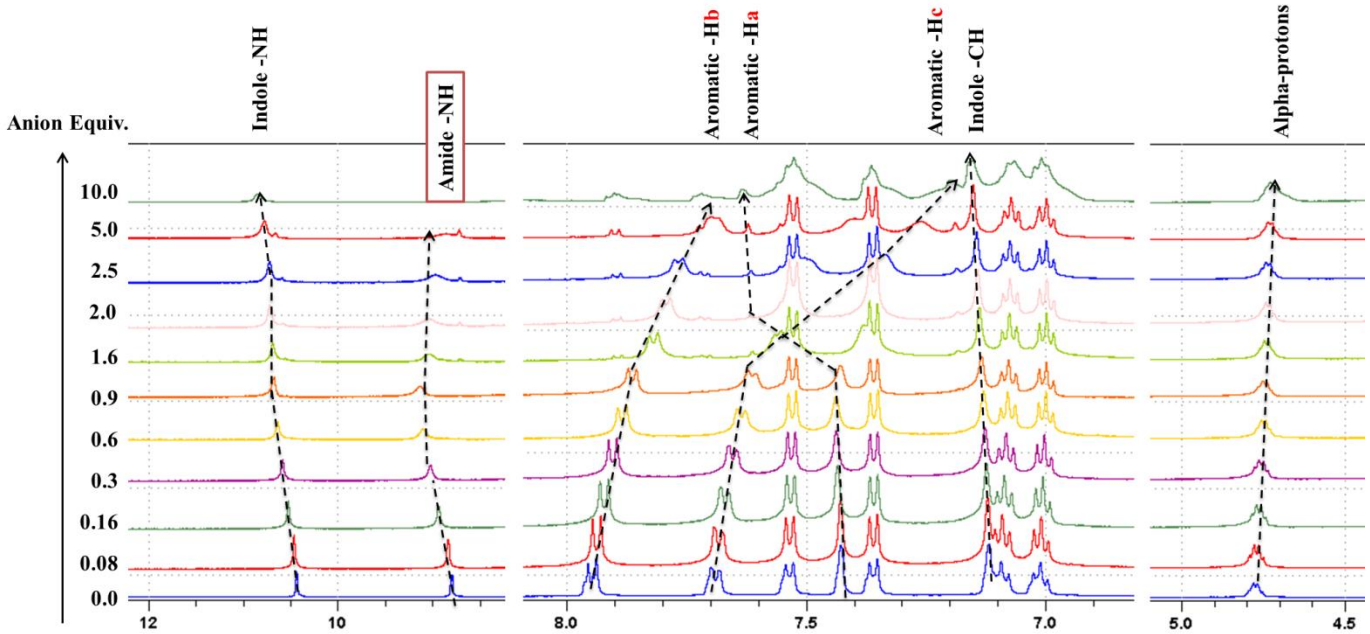

Figure S10: Stack plots of ^{1}H NMR spectra (500 MHz, CD_3CN:DMSO-d_6 9:1) of **W1** with increasing amount of TBAF. The region of protons involved in the binding is shown.

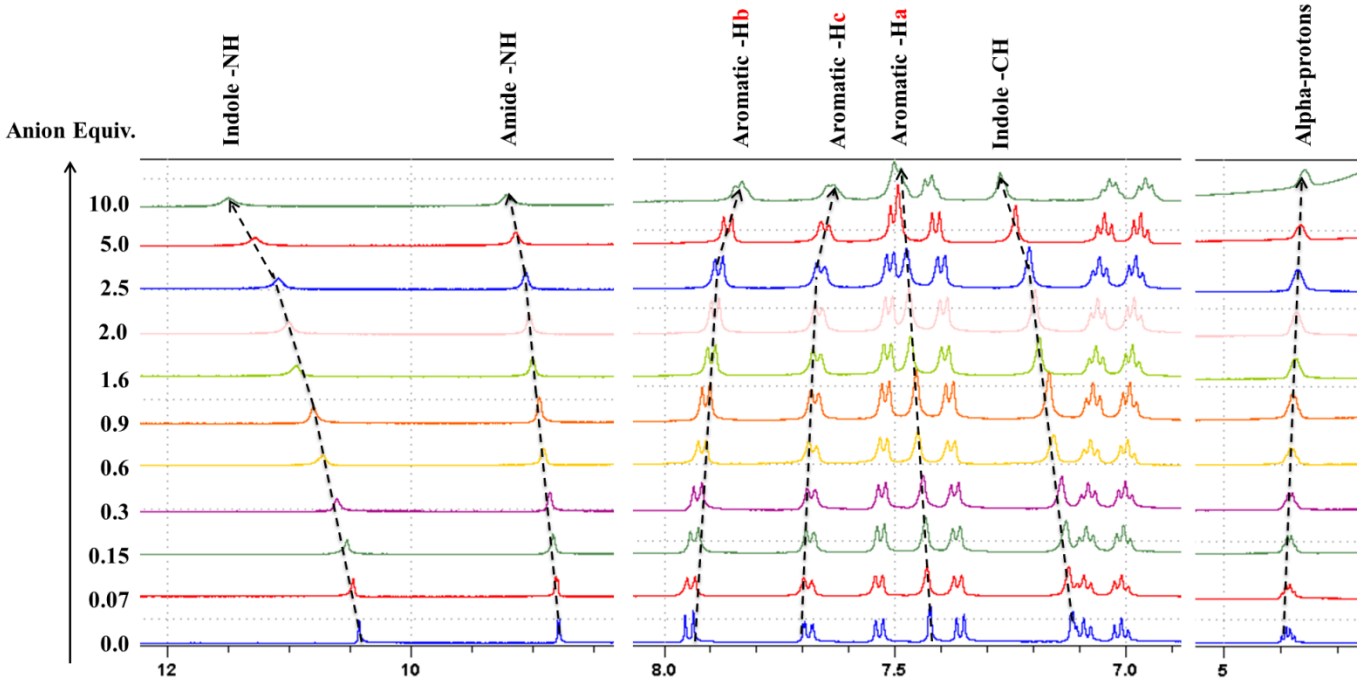

Figure S11: Stack plots of ^{1}H NMR spectra (500 MHz, CD_3CN:DMSO-d_6 9:1) of **W1** with increasing amount of $TBAH_2PO_4$. The region of protons involved in the binding is shown.

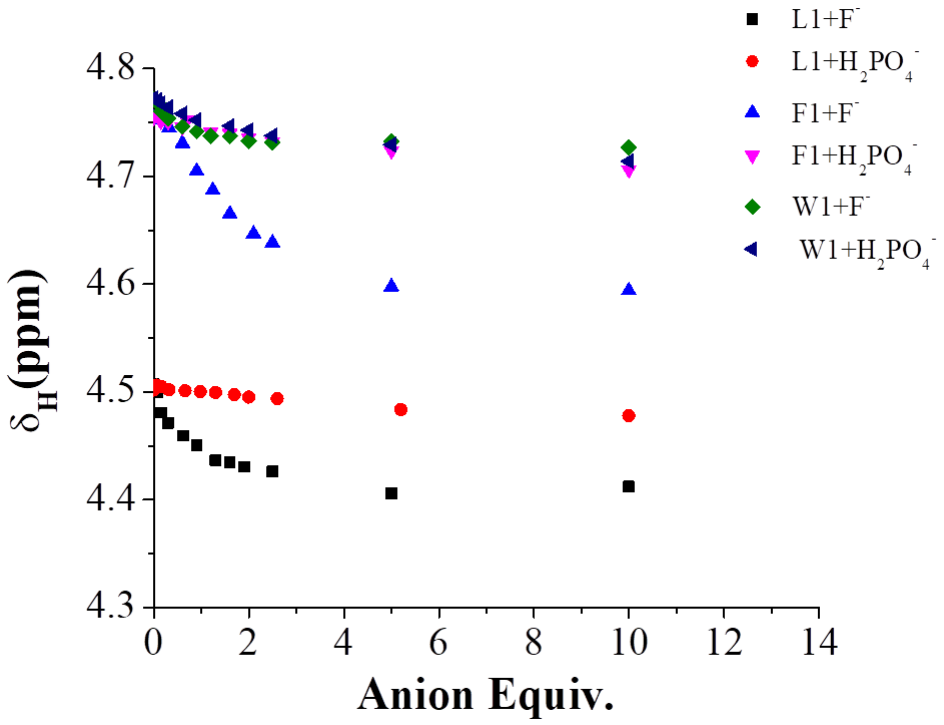

Figure S12: Variation in the ^{1}H NMR chemical shifts (δ ppm) of the alpha –CH as a function of equivalents of anions added.

a)

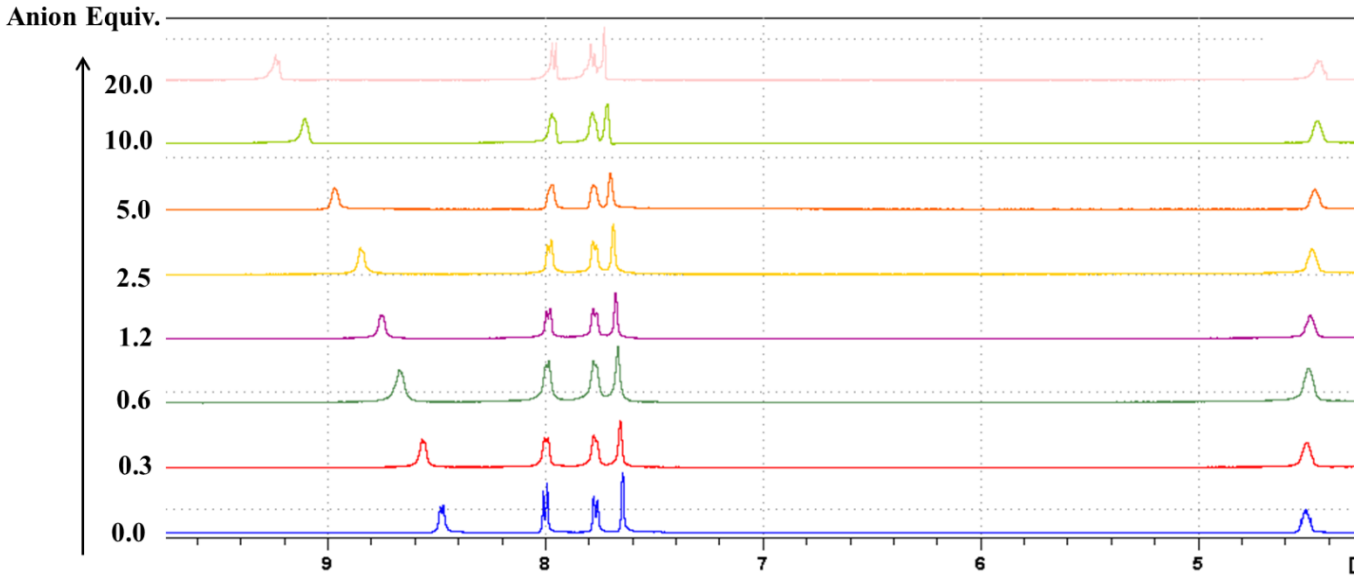

b)

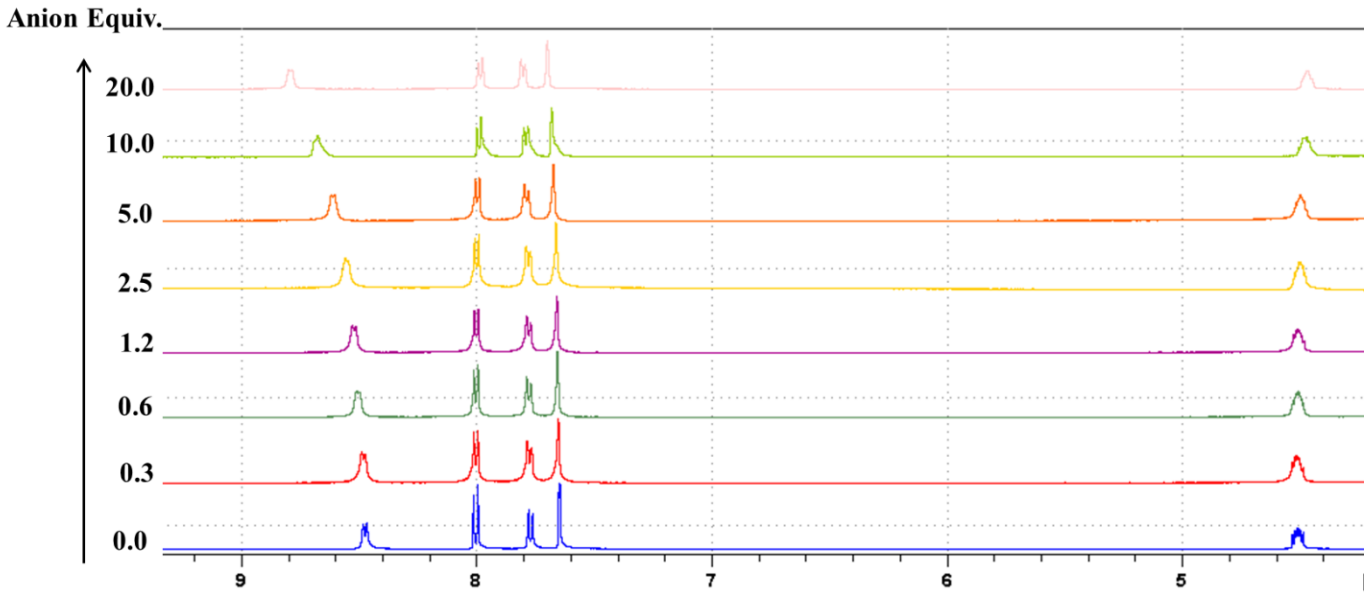

Figure S13: Stack plots of ^{1}H NMR spectra (500 MHz, CD_3CN:DMSO-d_6 9:1) of **L1** with increasing amount of a) TBACl, and b) TBABr.

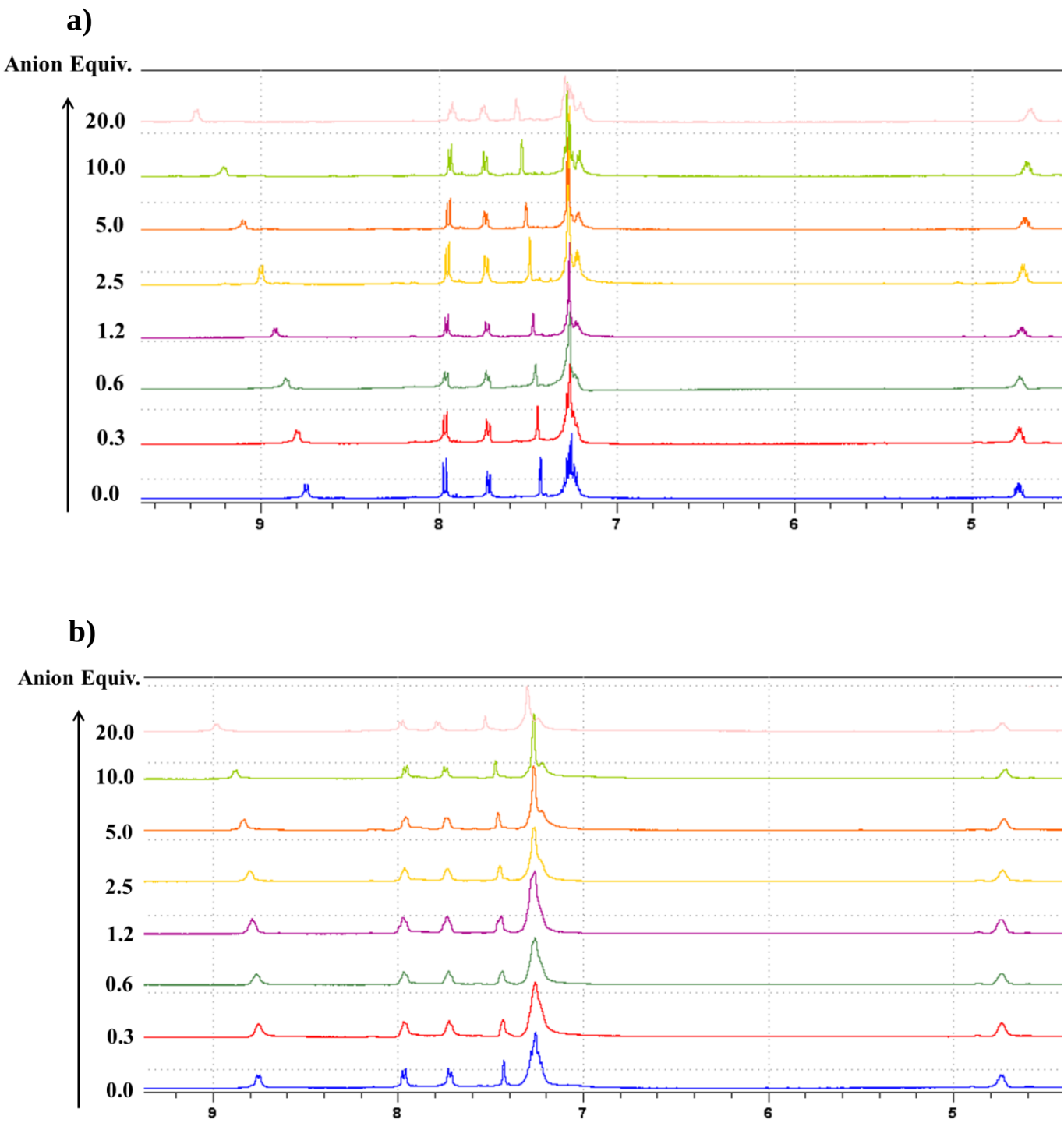

Figure S14: Stack plots of ^{1}H NMR spectra (500 MHz, CD_3CN:DMSO-d_6 9:1) of **F1** with increasing amount of a) TBACl, and b) TBABr.

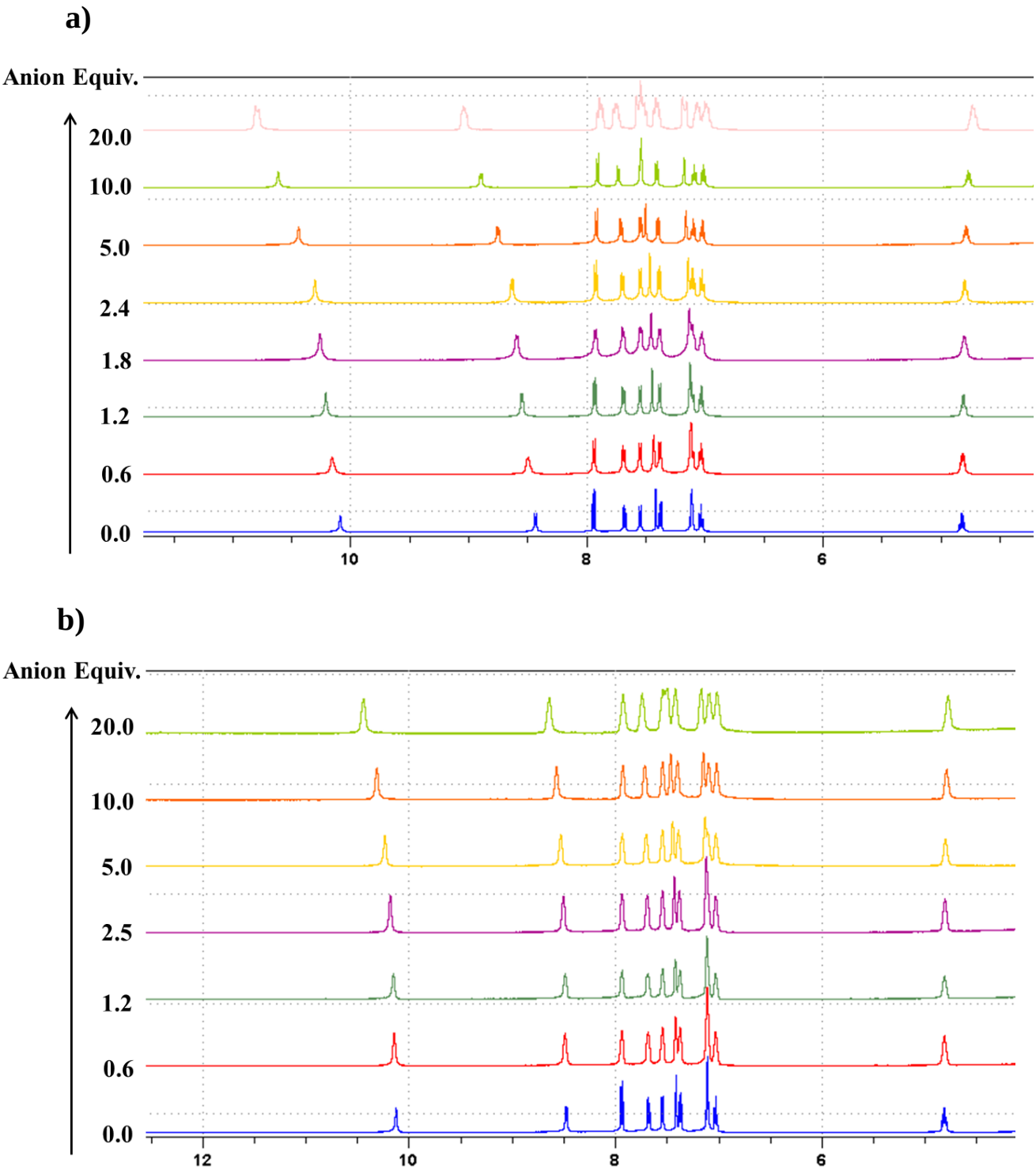

Figure S15: Stack plots of ^{1}H NMR spectra (500 MHz, CD_3CN:DMSO-d_6 9:1) of **W1** with increasing amount of a) TBACl, and b) TBABr.

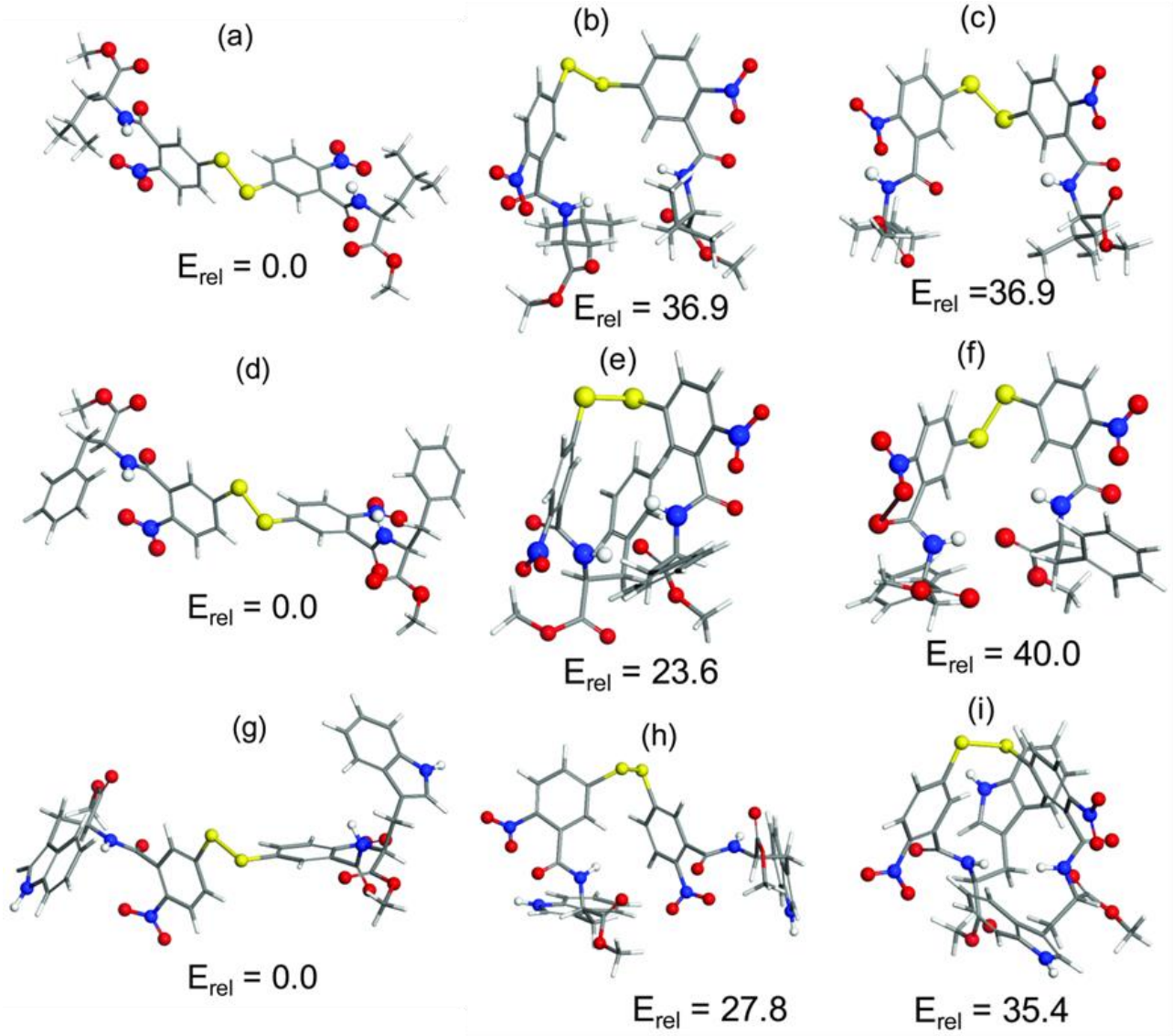

Figure S16: Optimized geometries of (a-c) **L1,** (d-f) **F1** and (g-i) **W1**, in folded- and extended-conformations. Relative energy (E_{rel}) of the structure is mentioned in kJ/mol. Color code: Sulfur (yellow), Nitrogen (blue), Carbon (silver), Oxygen (red), Hydrogen (white).

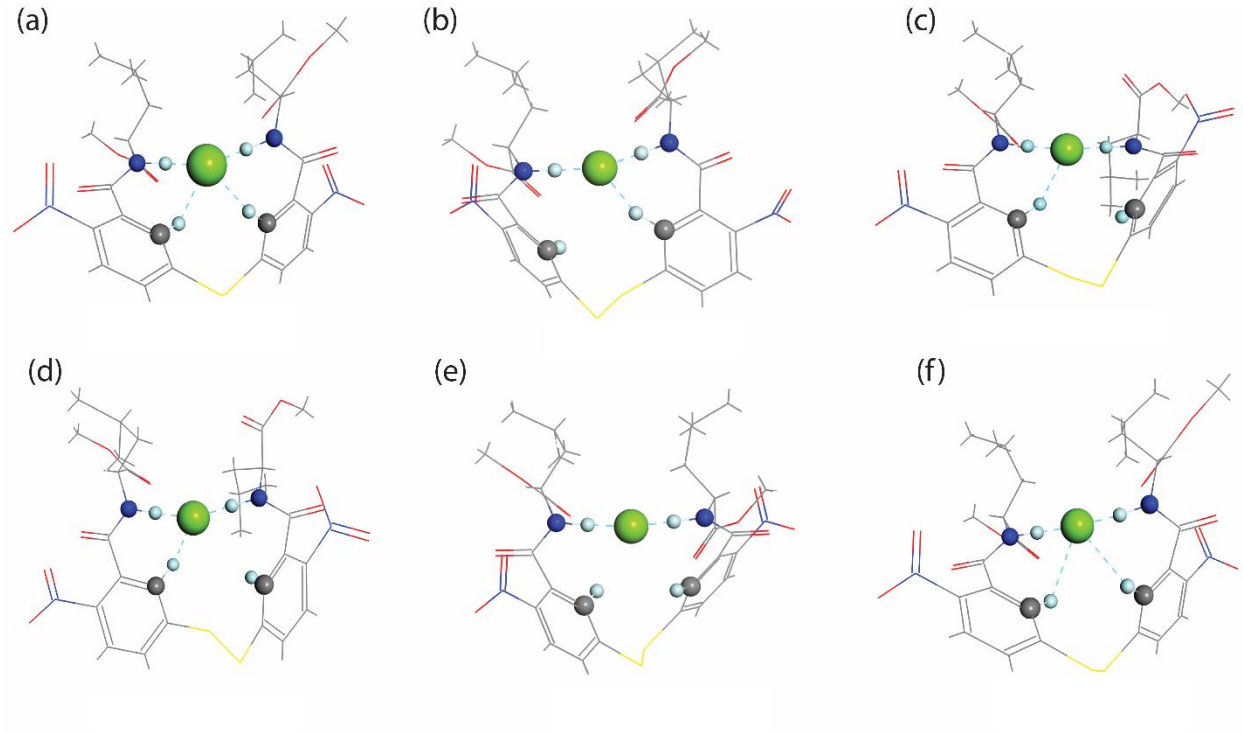

Figure S17: Structure pool of DFT optimized geometries of **L1+** F^- complexes having E_{rel} of a) 0.0 kJ/mol, b) -0.2 kJ/mol, c) -7.8 kJ/mol, d) -8.4 kJ/mol, e) -11.6 kJ/mol, and f) -8.5 kJ/mol. Color code: Sulfur (yellow), Nitrogen (blue), Carbon (silver), Oxygen (red), Hydrogen (white), Fluorine (green). Hydrogen atoms involved in H-bonding with anion are presented in sky-blue color.

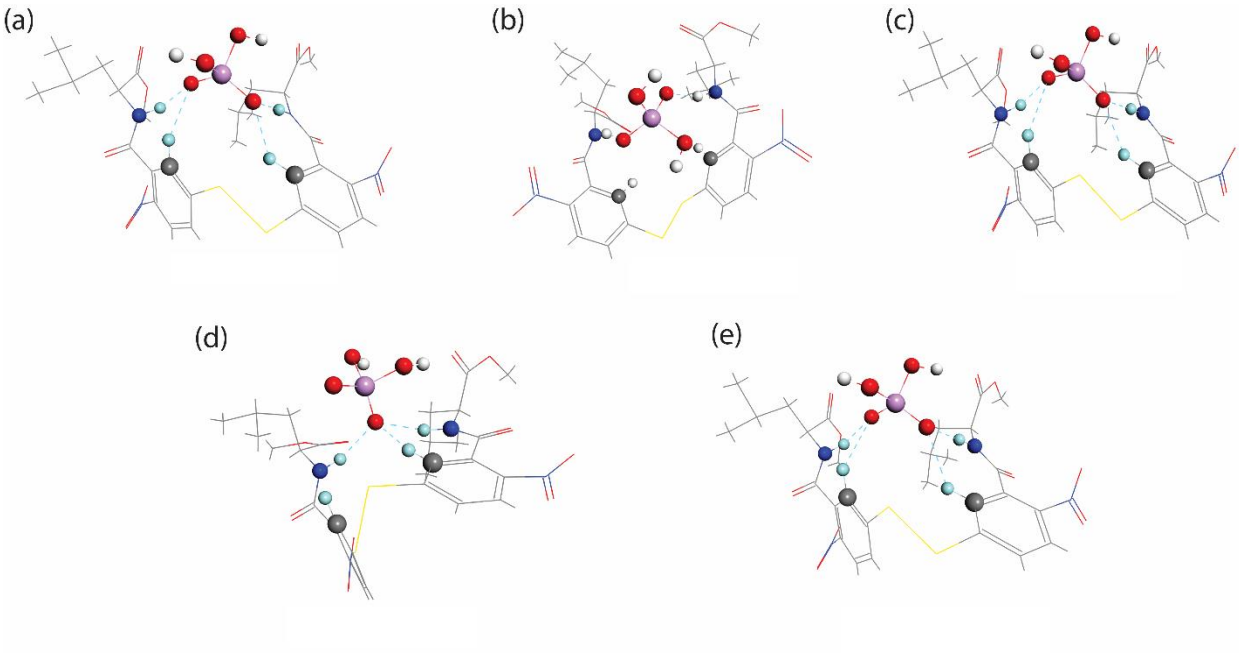

Figure S18: Structure pool of DFT optimized geometries of **L1**+$H_2PO_4^-$ complex having E_{rel} of a) 0.0 kJ/mol, b) 0.2 kJ/mol, c) 0.7 kJ/mol, d) 17.8 kJ/mol, and e) -1.5 kJ/mol. Color code: Sulfur (yellow), Nitrogen (blue), Carbon (silver), Oxygen (red), Hydrogen (white), Phosphorus (purple). Hydrogen atoms involved in H-bonding with anion are presented in sky-blue color.

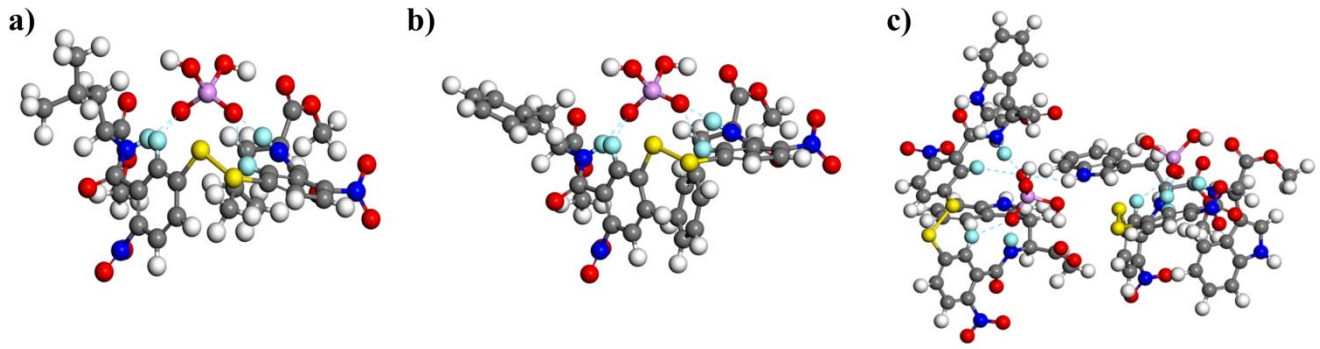

Figure S19: Optimized geometries of host-guest complex of $H_2PO_4^-$ anion with a) **L1**, b) **F1** and c) **W1**. Color code: Sulfur (yellow), Nitrogen (blue), Carbon (silver), Oxygen (red), Hydrogen (white), Phosphorus (purple). Hydrogen atoms involved in H-bonding with anion are presented in sky-blue color.

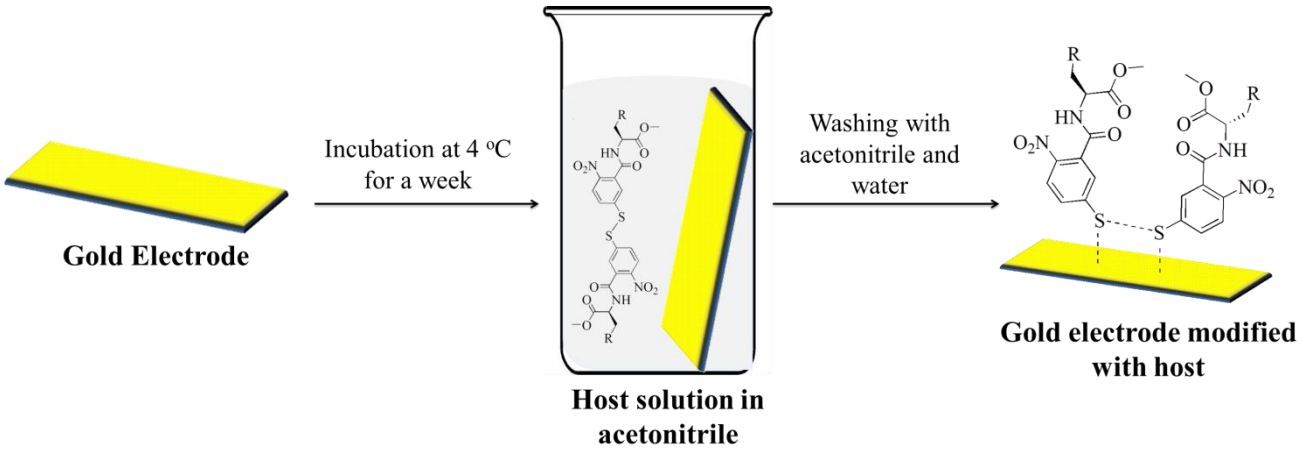

Figure S20: Schematic representation of the various steps involved in the fabrication of electrochemical sensor.

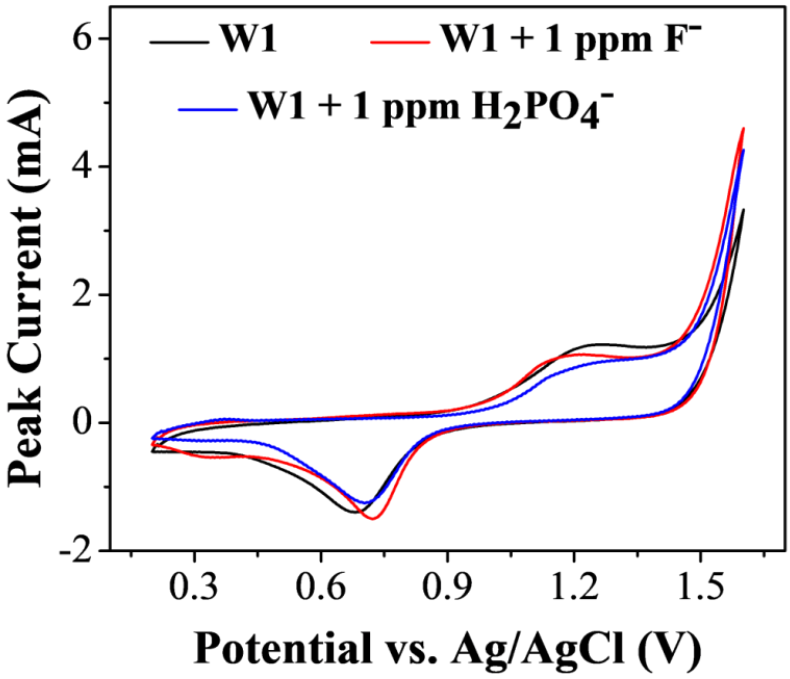

Figure S21: CVs obtained for the gold electrodes modified with **W1** in the absence and presence of 1 ppm of F^- and $H_2PO_4^-$ ions. Scan rate: 100 mVs^{-1}, Supporting Electrolyte: 0.1 M $NaNO_3$.

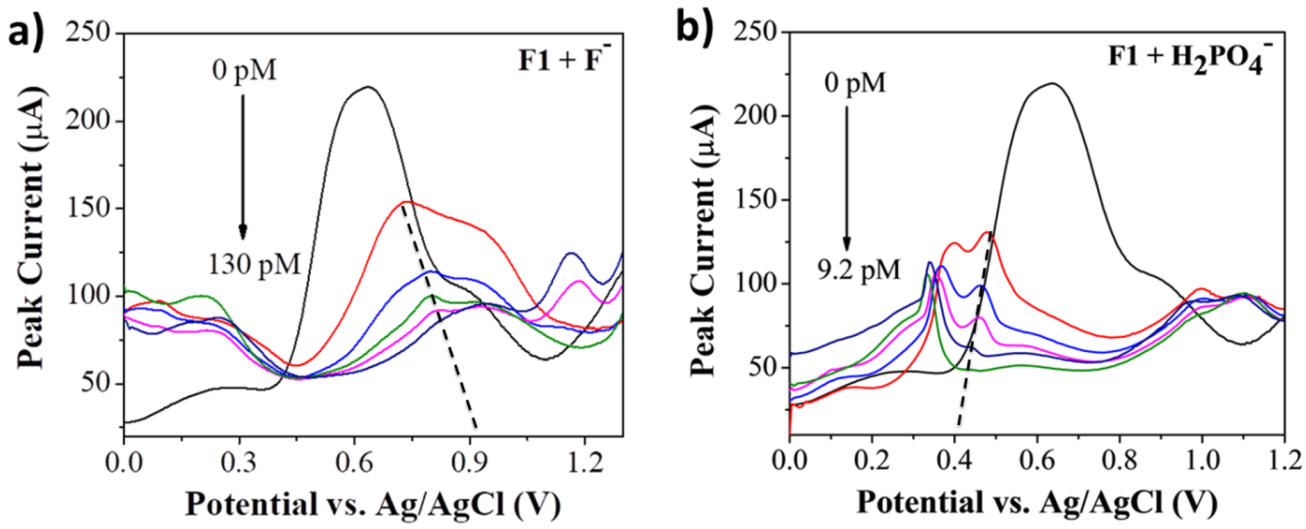

Figure S22: Differential pulse voltammograms obtained for the gold electrodes modified with **F1** with the varying concentration of a) F^- and b) $H_2PO_4^-$ ions.

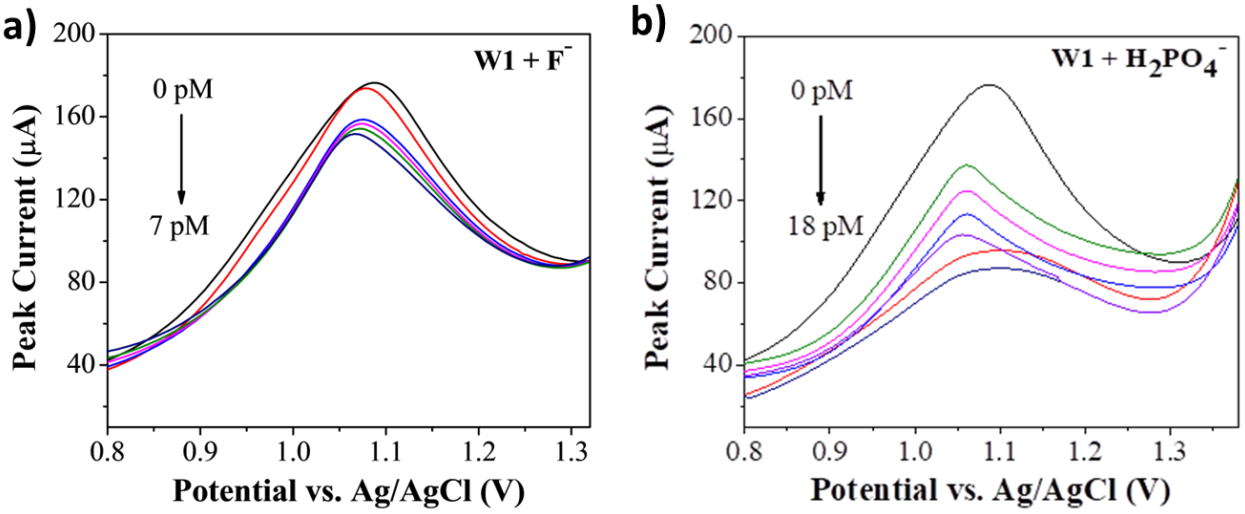

Figure S23: Differential pulse voltammograms obtained for the gold electrodes modified with **W1** with the varying concentration of a) F^- and b) $H_2PO_4^-$ ions.

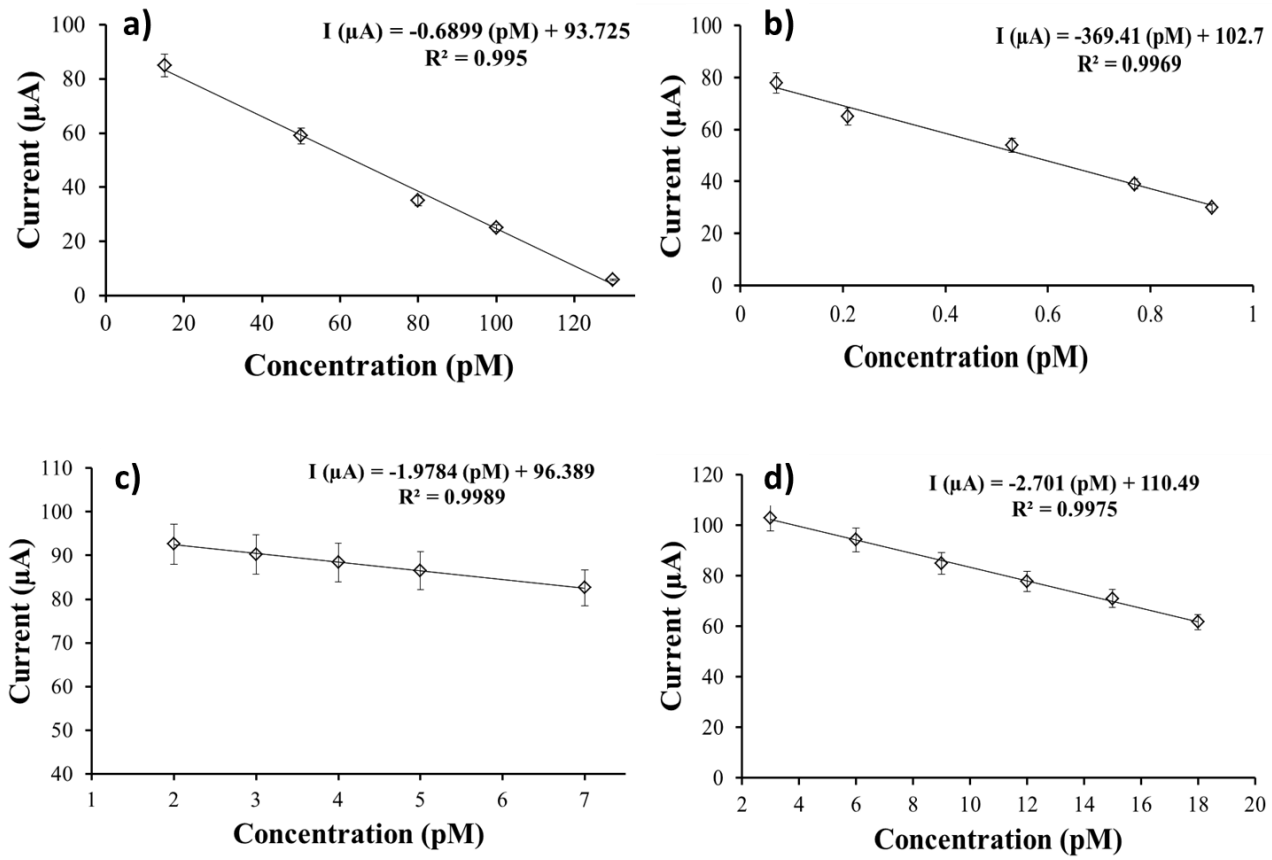

Figure S24: Plots of difference in redox current intensities with respect to anion concentration a) **F1** with F^-, b) **F1** with $H_2PO_4^-$ (peak current values were taken as marked in Figure S23), c) **W1** with F^-, d) **W1** with $H_2PO_4^-$ with a linear fit.

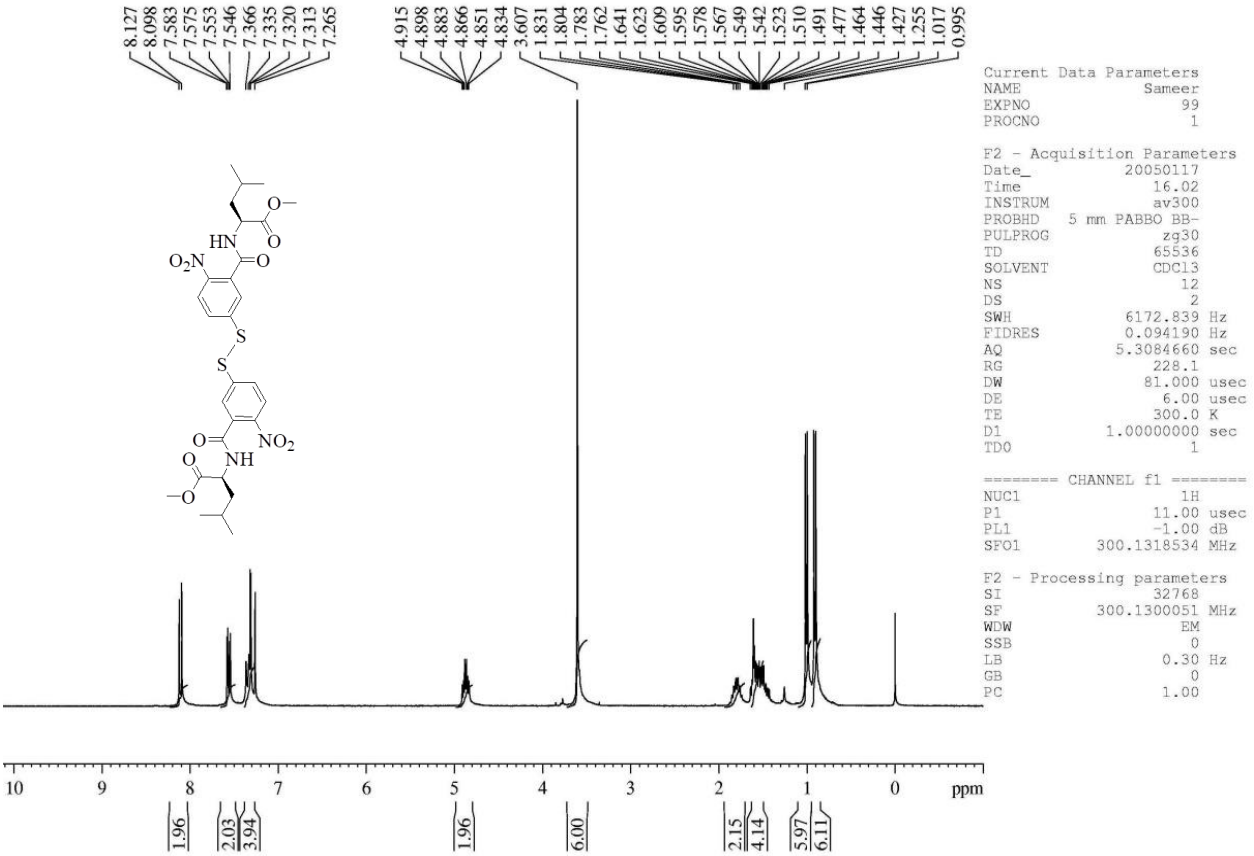

Figure S25: ^{1}H NMR spectrum (300 MHz, $CDCl_3$) of **L1**.

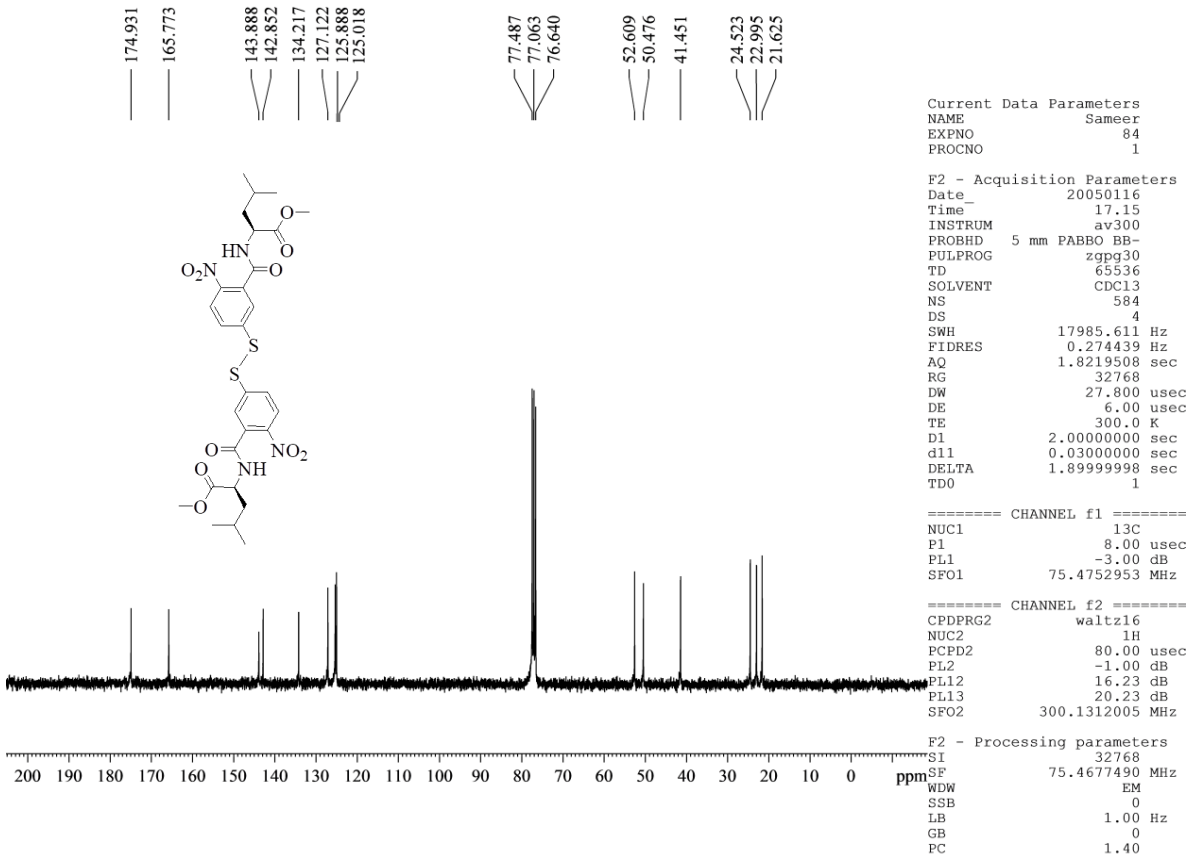

Figure S26: ^{13}C NMR spectrum (75 MHz, $CDCl_3$) of **L1**.

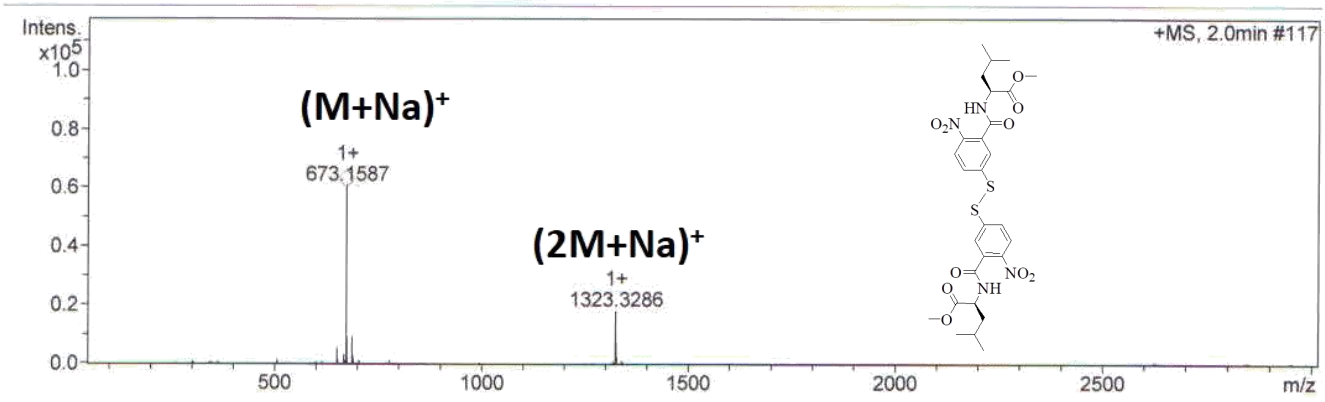

Figure S27: ESI-Mass spectrum of **L1**.

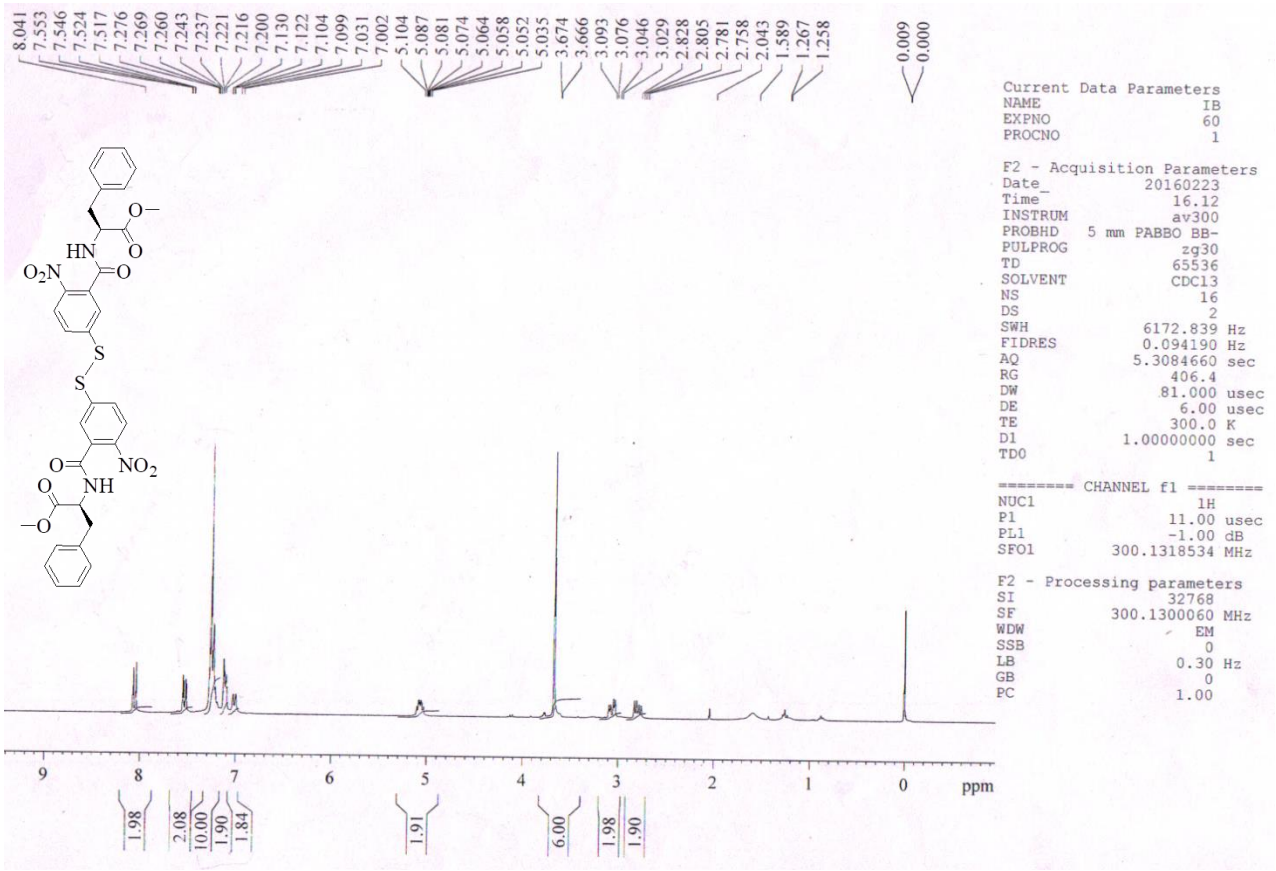

Figure S28: ^{1}H NMR spectrum (300 MHz, $CDCl_3$) of **F1**.

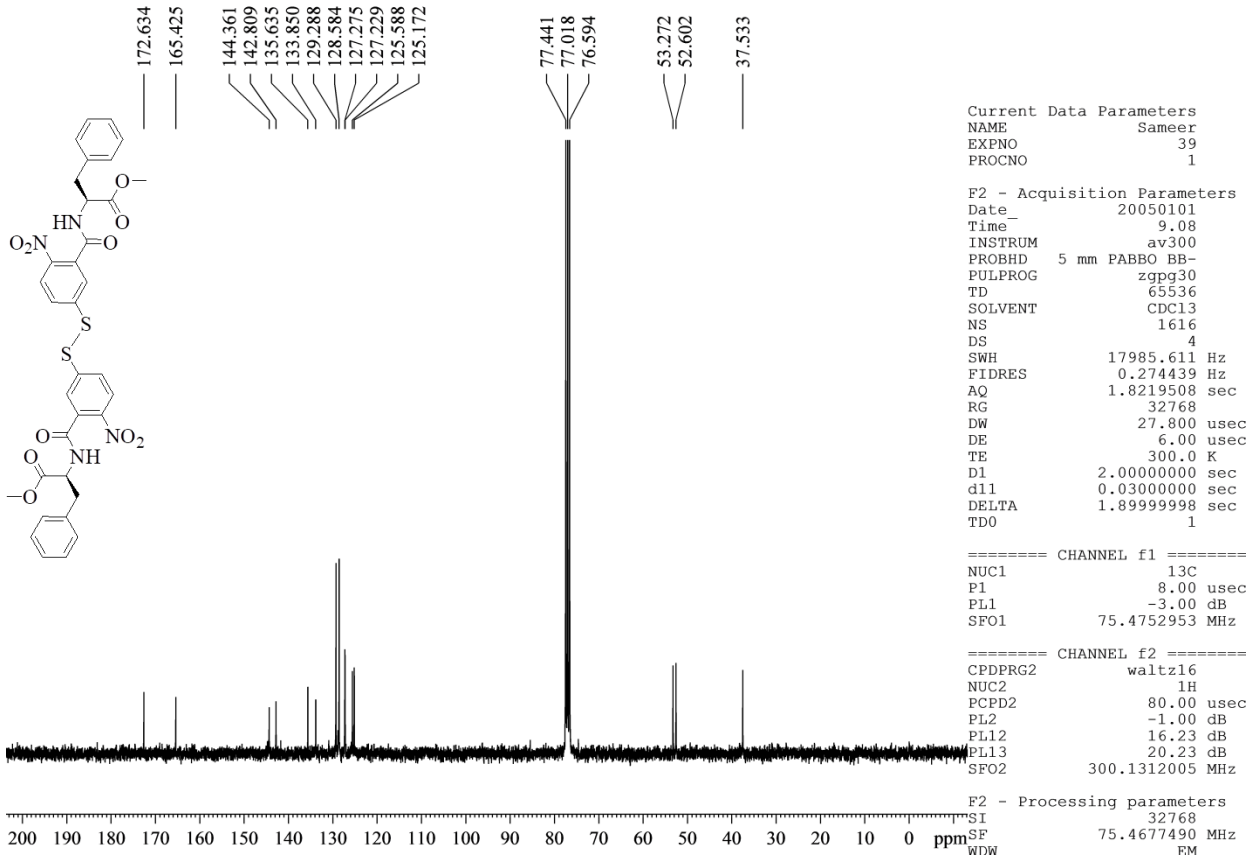

Figure S29: ^{13}C NMR spectrum (75 MHz, $CDCl_3$) of **F1**.

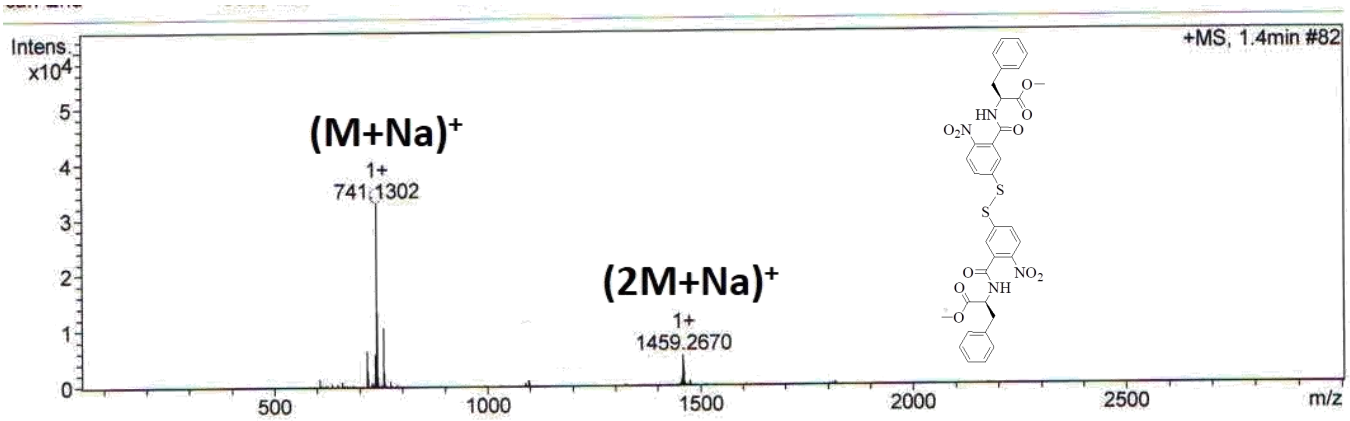

Figure S30: ESI-Mass spectrum of **F1**.

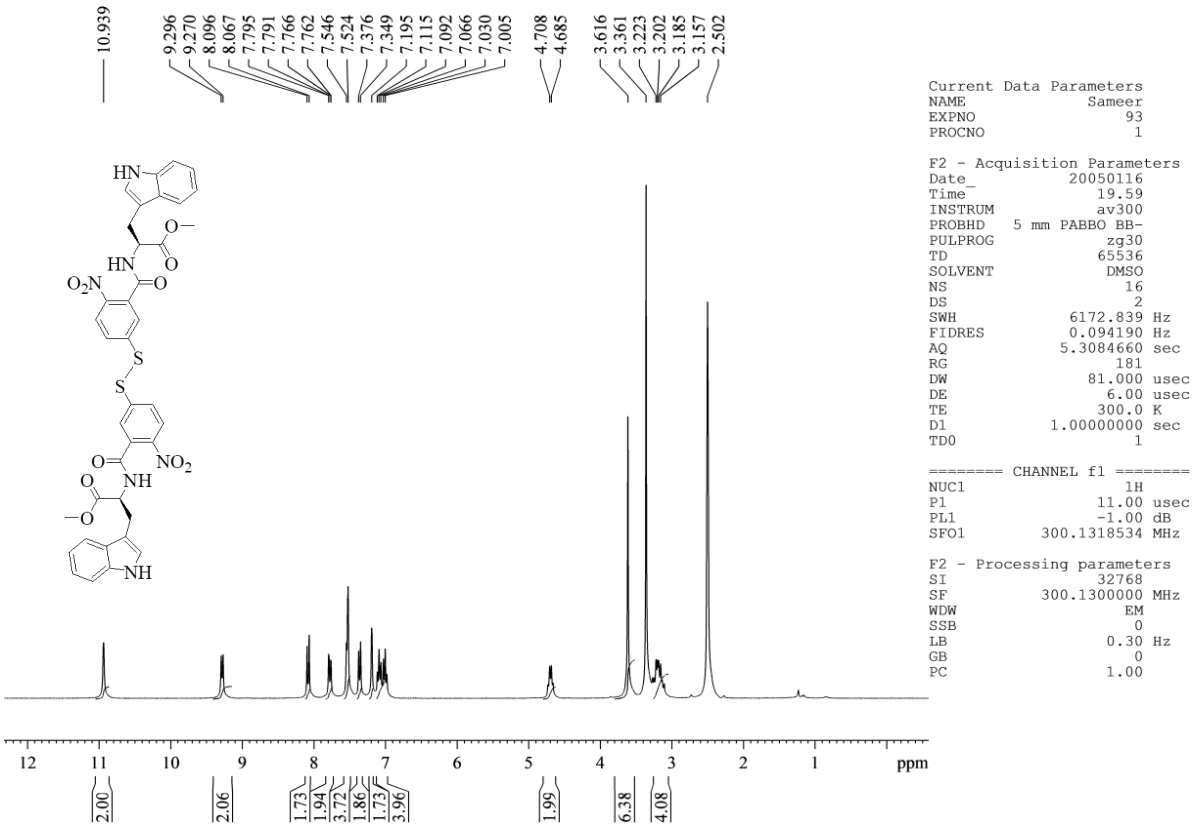

Figure S31: ^{1}H NMR spectrum (300 MHz, DMSO-d_6) of **W1**.

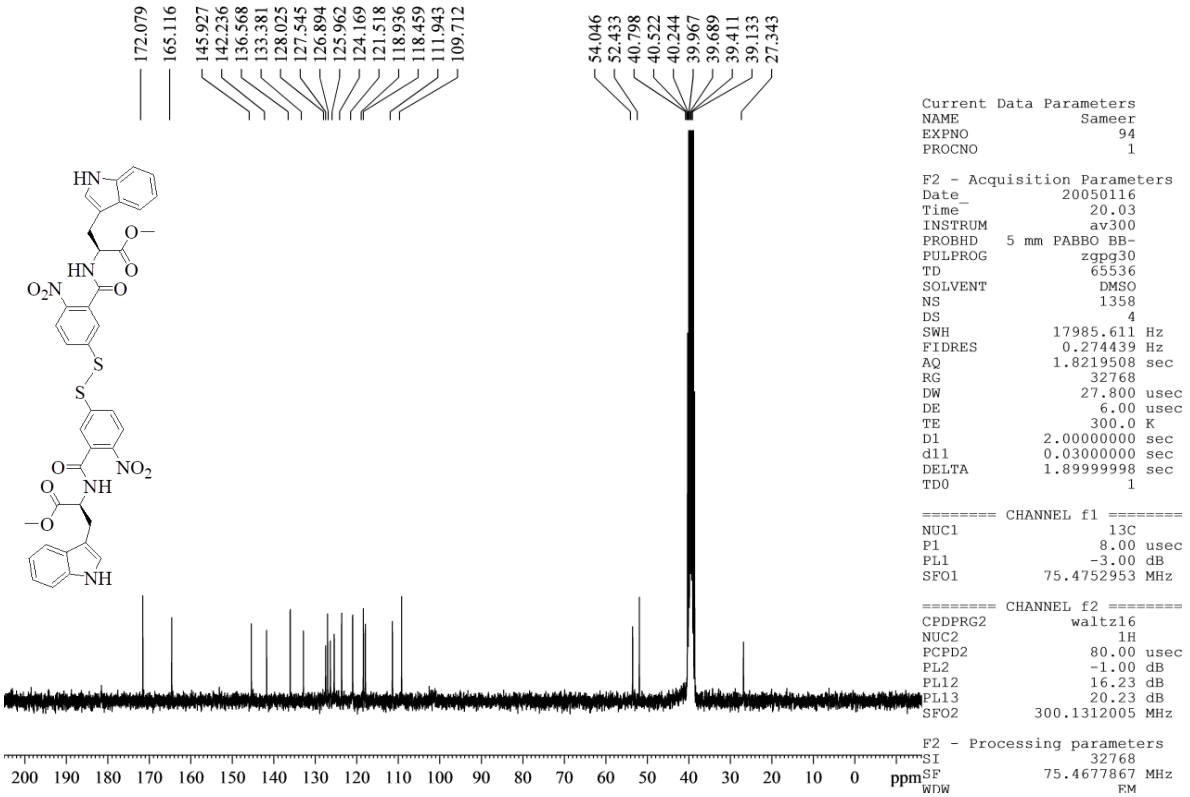

Figure S32: ^{13}C NMR spectrum (75 MHz, DMSO-d_6) of **W1**.

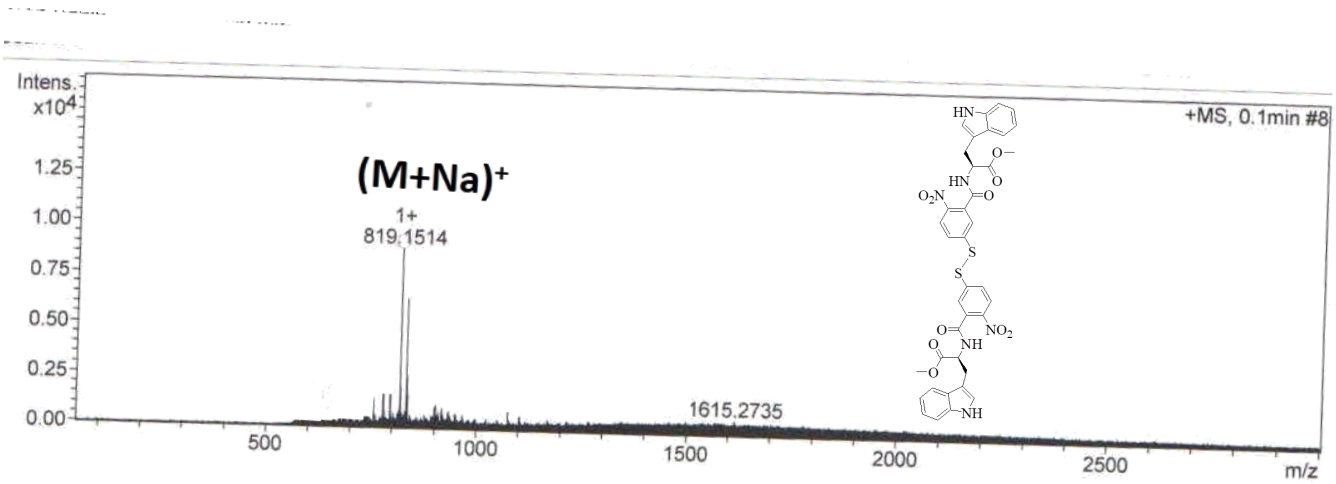

Figure S33: ESI-Mass spectrum of **W1**.

Table S1: Mulliken charges on the different H atoms of host molecules as derived from the most stable host-guest geometry.

Charge on H-atom	**L1**	**L1+F^-**	**L1 + $H_2PO_4^-$**	**F1**	**F1 +F^-**	**F1 + $H_2PO_4^-$**	**W1**	**W1 + F^-**	**W1 + $H_2PO_4^-$**
Amide -NH (1)	0.253	0.355	0.313	0.255	0.36	0.316	0.250	0.327	0.319
Amide -NH (2)	0.259	0.354	0.316	0.253	0.359	0.316	0.262	0.336	0.324
H_a(1)	0.151	0.171	0.185	0.136	0.162	0.153	0.145	0.162	0.148
H_a(2)	0.141	0.172	0.156	0.145	0.164	0.076	0.146	0.164	0.182
H_b(1)	0.157	0.102	0.154	0.159	0.107	0.159	0.159	0.146	0.164
H_b(2)	0.158	0.103	0.157	0.159	0.107	0.156	0.158	0.161	0.157
H_c(1)	0.132	0.082	0.142	0.137	0.084	0.139	0.137	0.132	0.143
H_c(2)	0.138	0.082	0.137	0.137	0.084	0.143	0.136	0.125	0.143
Indole –NH							0.238	0.289	0.277
Indole –CH							0.019	0.095	0.098

Table S2: Oxidation and reduction peak potentials (E) and current values (I) of the gold electrodes modified with host molecules.

Parameters	**L1**	**F1**	**W1**
$E_{oxidation}$ (V)	0.588	0.647	1.211
$I_{oxidation}$ (mA)	0.306	0.137	0.380
$E_{reduction}$ (V)	0.515	0.566	0.678
$I_{reduction}$ (mA)	0.297	0.127	0.985

Table S3: Oxidation peak potential values of modified gold electrodes in the absence (E^o_{free}) and presence of target anions (E^o_{bound}). Measuring conditions are mentioned in Figure 5 caption.

Anions	**L1**		**F1**		**W1**	
	E^o_{free} (V)	E^o_{bound} (V)	E^o_{free} (V)	E^o_{bound} (V)	E^o_{free} (V)	E^o_{bound} (V)
F^-	0.588	0.620	0.647	0.620	1.211	1.164
$H_2PO_4^-$	0.588	0.571	0.647	0.546	1.211	1.240

Table S4: Reduction peak potential values of modified gold electrodes in the absence (E^o_{free}) and presence of target anions (E^o_{bound}). Measuring conditions are mentioned in Figure 5 caption.

Anions	**L1**		**F1**		**W1**	
	E^o_{free} (V)	E^o_{bound} (V)	E^o_{free} (V)	E^o_{bound} (V)	E^o_{free} (V)	E^o_{bound} (V)
F^-	0.515	0.510	0.566	0.610	0.678	0.725
$H_2PO_4^-$	0.515	0.503	0.566	0.490	0.678	0.703

Table S5: Comparison of the performance of as-prepared anion sensors with those reported in the literature.

Anion Receptor	Solvent	Anions	Concentration Range	Lowest Concentration	Ref.
Dipyrromethene modified dipodal receptor based on Cu (II)	Water	Cl^-	1.0 - 12.0 pM	1.0 pM	1
Dipyrromethene modified dipodal receptor based on Co (II)	Water	Cl^-	1.0 - 12.0 pM	1.1 pM	1
Polypyrrole film modified electrodes	Water	F^- Cl^-	10^{-6} - 10^{-3} M 10^{-7} - 10^{-2} M	10^{-6} M 10^{-7} M	2
Ferrocene-appended aryl triazole	CH_2Cl_2	$H_2PO_4^-$	0.08 - 0.36 mM	0.08 mM	3
Diaminobutane poly(propyleneimine) dendrimer functionalized with biferrocenyl	CH_2Cl_2	$H_2PO_4^-$	0.1 - 7.77 μM	0.1 μM	4
1,2,3,4,5-Pentaphenylferrocene-stoppered rotaxane	CH_2Cl_2: CH_3CN	Cl^-	0.25 - 5 mM	0.25 mM	5
Tetratriazole foldamer	Water	I^-	-	14 μM	6
Sodium cellulose sulfate/poly(dimethyl diallyl ammonium chloride) composite	Phosphate buffer saline	NO_2^-	10^{-8} - 10^{-4} M	43 nM	7
Proline-based cyclopeptide + 6-mercapto-1-hexanol	Phosphate Buffer	SO_4^{2-}	0.5 - 2.0 pM	0.25 pM	8
Nitrogen-doped cotton carbon fiber composites	PBS	$O_2^{\cdot -}$	10^{-15} - 10^{-5} M	2.32 fM	9
L1	Water	$H_2PO_4^-$ F^-	0.07 - 0.50 pM 15.0 - 685.0 pM	0.07 fM 0.16 pM	This Work
F1	Water	$H_2PO_4^-$ F^-	0.07 - 0.92 pM 15.0 - 130.0 pM	0.15 fM 0.07 pM	This Work
W1	Water	$H_2PO_4^-$ F^-	3.0 - 18.0 pM 2.0 - 7.0 pM	0.02 pM 0.03 pM	This Work

References:

1. Kaur, B.; Erdmann, C. A.; Daniëls, M.; Dehaen, W.; Rafiński, Z.; Radecka, H.; Radecki, J. Highly Sensitive Electrochemical Sensor for the Detection of Anions in Water Based on a Redox-Active Monolayer Incorporating an Anion Receptor. *Anal. Chem.* **2017**, *89*, 12756–12763.
2. Lou, B.; Chen, C.; Zhou, Z.; Zhang, L.; Wang, E.; Dong, S. A Novel Electrochemical Sensing Platform for Anions Based on Conducting Polymer Film Modified Electrodes Integrated on Paper-Based Chips. *Talanta* **2013**, *105*, 40–45.
3. Cao, Q.-Y.; Pradhan, T.; Kim, S.; Kim, J. S. Ferrocene-Appended Aryl Triazole for Electrochemical Recognition of Phosphate Ions. *Org. Lett.* **2011**, *13*, 4386–4389.
4. Villena, C.; Losada, J.; García-Armada, P.; Casado, C. M.; Alonso, B. Synthesis and Electrochemical Anion-Sensing Properties of a Biferrocenyl-Functionalized Dendrimer. *Organometallics* **2012**, *31*, 3284–3291.
5. Evans, N. H.; Serpell, C. J.; White, N. G.; Beer, P. D. A 1,2,3,4,5-Pentaphenylferrocene-Stoppered Rotaxane Capable of Electrochemical Anion Recognition. *Chem. - Eur. J.* **2011**, *17*, 12347–12354.
6. Hein, R.; Borissov, A.; Smith, M. D.; Beer, P. D.; Davis, J. J. A Halogen-Bonding Foldamer Molecular Film for Selective Reagentless Anion Sensing in Water. *Chem. Commun.* **2019**, *55*, 4849–4852.
7. Ning, J.; Luo, X.; Wang, M.; Li, J.; Liu, D.; Rong, H.; Chen, D.; Wang, J. Ultrasensitive Electrochemical Sensor Based on Polyelectrolyte Composite Film Decorated Glassy Carbon Electrode for Detection of Nitrite in Curing Food at Sub-Micromolar Level. *Molecules* **2018**, *23*, 2580.

8. Gołębiewski, P.; Sommer, F.; Kubik, S.; Radecka, H.; Radecki, J. Ion-Channel Mimetic Sensor Incorporating an Anion-Binding Cyclopeptide Designed for Sulfate Determination in Dilute Aqueous Solutions. *J. Electroanal. Chem.* **2018**, *812*, 249–257.
9. Wu, T.; Li, L.; Song, G.; Ran, M.; Lu, X.; Liu, X. An Ultrasensitive Electrochemical Sensor Based on Cotton Carbon Fiber Composites for the Determination of Superoxide Anion Release from Cells. *Microchim. Acta* **2019**, *186*. DOI: 10.1007/s00604-019-3304-1.